MODELLING OF PARTICLE COARSENING AND PRECIPITATION FREE ZONES

MODELLING OF PARTICLE COARSENING AND PRECIPITATION FREE ZONES

BY

NA YANG, B.Eng.

A THESIS
SUBMITTED TO THE DEPARTMENT OF MATERIALS SCIENCE AND ENGINEERING
AND THE SCHOOL OF GRADUATE STUDIES
OF MCMASTER UNIVERSITY
IN PARTIAL FULFILMENT OF THE REQUIREMENTS
FOR THE DEGREE OF
MASTER OF APPLIED SCIENCE

Master of Applied Science (2015)
(Materials Science and Engineering)

McMaster University
Hamilton, Ontario, Canada

TITLE: MODELLING OF PARTICLE COARSENING AND PRECIPITATION FREE ZONES

AUTHOR: Na Yang
B.Eng., (Materials Science and Engineering)
University of Science and Technology Beijing, Beijing, China

SUPERVISOR: Dr. Jeffrey J. Hoyt

NUMBER OF PAGES: x, 74

To my mother Haiying Liu, my uncle Xuefeng Xu and my grandparents on my mother's side, Jingui Liu and Xiuyun Li

Abstract

Starting with the Mean Field Method (MFM) and Boundary Element Method (BEM), we investigate a mathematical model based on these two methods for studying particle-coarsening process in alloys. With MFM, second-phase particles are considered to be merged into bulk matrix, which greatly simplifies computation. However, the Mean-Field model itself is limited to a system with extremely small volume fractions of second phase. By combining BEM with MFM, this mathematical model shows the influence of second phase in particle-coarsening process. Our primary work demonstrates the robustness and capability of this model. This model is however limited to particle coarsening that is far away from grain boundaries.

In this dissertation, we successfully extend the model to particle coarsening near grain boundaries. A major improvement made to the previous mathematical model is based on solute atoms conservation and diffusion theory. The capability and validity of the novel model is demonstrated by a binary alloy system. The simulation results are shown to quantitatively reproduce the essential features of particle coarsening near grain boundaries in certain alloys: a) precipitation Free Zones (PFZs) form near grain boundaries, b) the width of PFZs is proportional to square root of time, c) particles at the edge of PFZs are larger than those inside the grain.

This novel model is shown to be well suited in describing particle coarsening near grain boundaries. On the other hand, it proves the credibility of the theories built in our mathematical model, i.e., the formation of PFZs near grain boundaries is caused by diffusion of solute atoms.

Acknowledgements

The contributions from a number of people are beneficial to the completion of this thesis.

First and foremost, the author wishes to express her utmost gratitude to her supervisor, Dr. Jeffrey J. Hoyt. For the past three years, Dr. Hoyt has been a great mentor of the author without fail or hesitation since the author first came to McMaster University as a senior undergraduate student and then again a couple of years later as Master student. He is such a remarkable person and professor that his guidance, advice, insight, enthusiasm and expertise are second to none.

Very special thanks must be given to her group members, Peyman Saidi, Huajing Wilson Song and Tara Power. Their creative suggestions and helpful advices are greatly appreciated.

The author would like to thank her friends, Jianting Yue, Hongmei Cheng, Jingjing Xin and Xu Jiao for their encouragement.

Finally and most importantly, the author would like to thank her mother Haiying Liu, her uncle Xuefeng Xu and her grandparents on her mother's side Jingui Liu and Xiuyun Li for their unconditional and endless love and support.

The financial support of Novelis company, and computing resources from Sharcnet and BHP are also acknowledged.

Contents

List of Figures

List of Tables

Chapter 1

Introduction

The performance of most alloys is largely dependent on their microstructures. There have been lots of researches regarding the growing and coarsening of grains in polycrystalline materials, which are of great significance in studying the properties of these materials. As a common sense, precipitates free zones (PFZs) exist in several alloys, whereas the formation mechanism of PFZs is still under intensive discussion. Due to the high temperature required in the coarsening process of grains, the boundaries of grains evolve in an unbalanced fashion, which makes it difficult to directly observe how microstructures change. From this point of view, modelling is a useful as well as practical approach. In this dissertation, a model combining Mean Field Method (MFM) and Boundary Element Method (BEM) is used to study particle coarsening and PFZs.

1.1 Particle coarsening

1.1.1 Effects of particle coarsening

Particle coarsening has significant influence on mechanical properties and deformation characteristics of crystalline materials especially for magnesium alloys, aluminum alloys and nickel alloys.

It is crucial to inhibit particle coarsening in magnesium casting alloys. Particle coarsening can be induced leading to shrinkage and hot defects in alloys. It is worthwhile to point out here that adverse effects are especially obvious for magnesium alloys. Inhibition of particle coarsening is a technology through controlling the morphology and distribution of the second phase to produce high quality magnesium alloys [1, 2]. Since magnesium alloys have a wide range of crystallization temperature, low thermal conductivity and large volume shrinkage ratio, they are of great tendency of particle coarsening. At the same time, magnesium alloys have close-packed hexagonal structure, which means there are only four independent slip systems. This is another reason why particle size is of great influence on the mechanical properties. It turns out that inhibition of particle coarsening could effectively control the shrinkage and the enlargement of the second phase, and thus improve the mechanical properties and air impermeability of casting alloys. In the mean time, it controls the increase of diffusion distance of solid solution (such as $Mg_{17}Al_{12}$), and thus improves the efficiency of heat treatment and corrosion resistance of casting alloys [3, 4].

Aluminum alloys have been generally applied in transportation, chemical industry [5], mechanical industry [6], electrical industry, construction [7] and so on, in the sense that higher requirements of their performance and microstructure are put forward. Most of aluminum alloys are produced through melting and casting, namely going through the crystallization process from liquid to solid [8, 9]. As a consequence, metal products form microstructures with all kinds of particle size and distribution, which greatly affects the processing performance and mechanical properties of these products. And it is the key point to produce fine and uniform precipitates. Obviously, inhibition of particle coarsening can improve the strength of aluminum alloys [10].

Nickel based superalloy single crystals have been playing key roles in high temperature gas turbine applications over the past decades. The morphology of γ' precipitate in these alloys has shown considerable influence on high temperature creep properties [11, 12]. Low coarsening rate of the initial γ' is preferred, since fine γ' dispersion is more ready than aged precipitates in creep conditions [13, 14, 15]. Some researchers proposed that γ' precipitate coarsens in a diffusion controlled mechanism [16, 17]. However, due to the lack of experimental data, arguments still exist.

1.1.2 Why particle coarsening happens?

Particles or precipitates of second phase are usually considered as spheres in many theories of particle coarsening [18, 19, 20], which is a reasonable assumption from both theoretical and practical perspectives. Theoretically, interfacial energy in a sphere is lower than in any other shape with same volume, which helps the system maintain an equilibrium state [21]. Practically, a large number of researchers have detected that precipitates are spheres. Fährmann et al. [22] and Kim et al. [23] observed round precipitates in their microstructural examinations in Ni-Al-Mo alloys and Al based alloys, which means some precipitates exist in the shape of spheres. Furthermore, precipitates of second phase in Al-Li alloys are also shown to be spheres. Sanders and Starke stated that the misfit of second phase and matrix is as low as 0.18% due to sphere shape of second phase [24].

In order to give a brief illustration of particle coarsening, this section discusses a binary system with α matrix and β second phase. We assume that β precipitates are particles due to the reasons listed in the above paragraph. If and only if the chemical potential of each species is equal in α matrix and β second phase and the pressure imposed on the particles of radius R is greater than that on surrounded α matrix, the extra pressure that is equal to chemical potentials is calculated by Gibbs-Thomson Eq. 1.1 [25, 26].

$$\Delta\mu_i^\beta = \frac{2\sigma\nu_i}{R} \tag{1.1}$$

where σ is interfacial energy and ν_i is the molar volume of species i in second phase β. As demonstrated in Gibbs-Thomson effect, chemical potential difference of a particle is dependent on its curvature since it is related to radius R. In addition, more details of the driving force of particle coarsening are illustrated in Figure 1.1 [27].

As shown in Figure 1.1, the biggest curve represents α matrix, and meanwhile two relatively small curves describes β phase. To be more specific, the lower curve is for the equilibrium state and the higher one is for a certain non-equilibrium state. Correspondingly, c_e is the equilibrium composition of α matrix and c_β is the composition of β phase. It is worth noting that only after a long time, the system could reach equilibrium state that the lower small curve represents. And under the

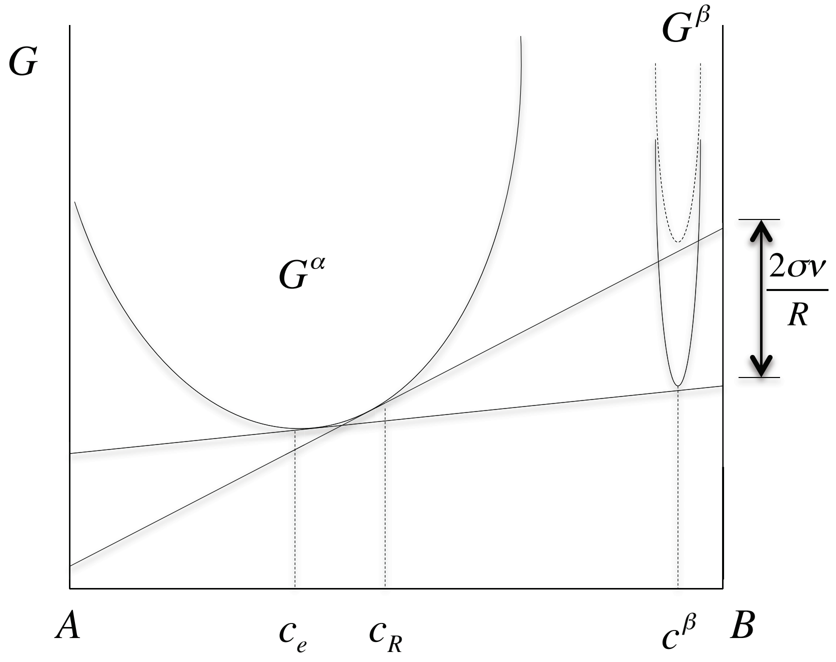

Figure 1.1: Gibbs free energy vs. composition for a binary system in equilibrium

equilibrium state, chemical potential difference $\Delta\mu_i^\beta = 0$ is achieved, which means particle radius R goes to infinity. In other words, there is not any sphere particles of β phase within a reasonable timeframe. In this case, interface between α matrix and β phase will be flat. Since this equilibrium state is hardly reached, more research interest focuses on non-equilibrium state where β phase are distributed in the matrix as sphere particles.

Due to Gibbs-Thomson effect, the Gibbs free energy of a sphere particle is higher than that in equilibrium state. Correspondingly, the concentration of matrix near this particle c_R is higher. Apparently, if a larger particle exhibits, c_R decreases as the radius of particle R increases. This relationship could be pinpointed by Eq. 1.2 [27].

$$c_R = c_e(1 + \frac{\Gamma}{R}) \tag{1.2}$$

where Γ is known as the *capillary length*, which is a constant dependent on materials and temperature. Eq. 1.2 could be better illustrated in Figure 1.2 [28].

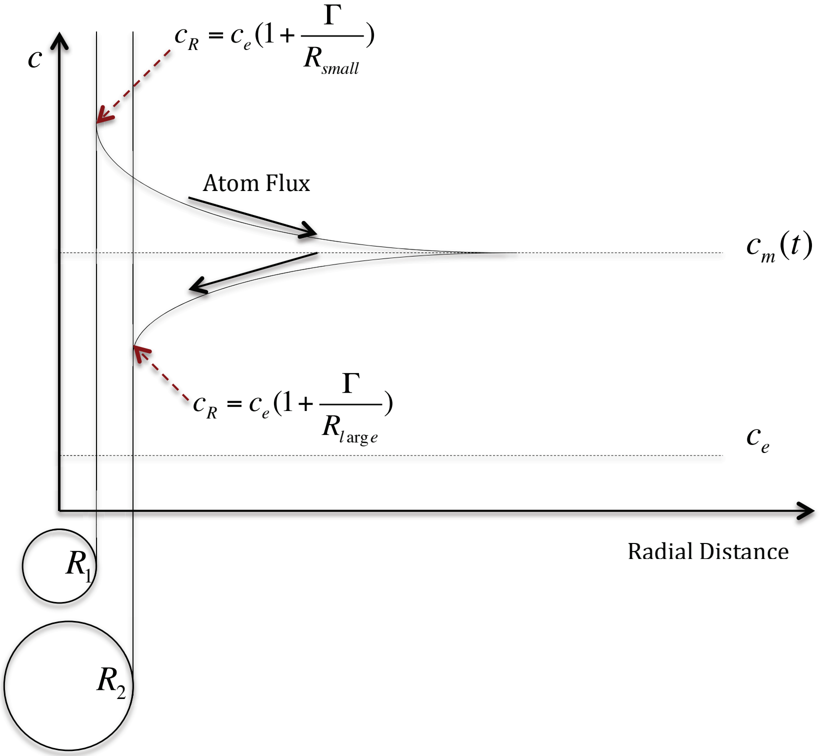

Figure 1.2: The concentration vs. radial distance in the matrix

$$c_m(t) = c_e(1 + \frac{\Gamma}{R_{critical}(t)}) \tag{1.3}$$

where $c_m(t)$ is average matrix concentration for any specified domain and $R_{critical}(t)$ is a critical particle size.

As shown in Figure 1.2, concentration of matrix around particles smaller than $R_{critical}(t)$ is large because of a small value of radius. Conversely, concentration of matrix around particles larger than $R_{critical}(t)$ is small because of a large value of radius. Particles with radius $R_{critical}(t)$ do not change their size at this moment. At the same time, solute atom fluxes surrounded different particles go in different trends due to concentration gradient. To be more specific, for matrix near small particles, there is an atom flux from small particles to matrix. In the meantime, for matrix near large particles, there is an atom flux to large particles. This phenomenon is shown in Figure 1.3, where the dotted circle means a specified domain in the matrix for a binary system exhibiting α matrix and β phase. The radius of this domain is known as cutoff distance. Notably, the center particle has interactions with another particle only if their distance is shorter than cutoff distance with the restriction of diffusion distance. In other words, the center particle has interactions with particles inside the sphere domain. If a particle in the domain is smaller than the center one, there will be atom flux from this particle to center particle, and vice versa. As a consequence, small particles shrink or even disappear while large particles grow. This process is called Ostwald ripening or particle coarsening [29, 30].

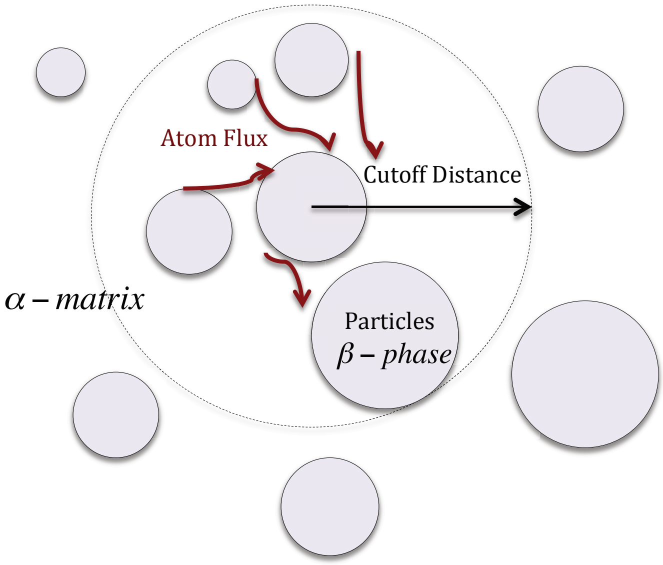

Figure 1.3: A microstructural illustration for a system exhibits α matrix and β phase

1.1.3 Theories of particle coarsening

In the turn of last century, Ostwald [29] first discovered the phenomena of particle coarsening. Since the early work of Ostwald, it is now well known that the driving force for particle coarsening process is the chemical potential that is dependent on particle curvature. Originally, attempts to explain the ripening process were only in qualitative sense. Greenwood [31] discussed theoretical aspects of particle coarsening quantitatively. However, the disadvantage in their theories is that the solution to main diffusion equation is unrealistic, which leads to a disagreement against experimental results.

Later, Lifshitz and Slyozov [32] and Wagner [33] successfully developed a theory which is known as LSW theory for quantitative predictions of particle coarsening. They assumed that particles of second phase are not only spheres but also fixed in matrix, which means centers of particles never change during coarsening process. At the same time, they ignored nucleation and particle coalescence. Based on the mass conservation and Fick's second law, through asymptotic analysis, they suggested that the average particle radius $\bar{R}$, matrix concentration c_m and the average particle number per unit volume N are all time t dependent over a long term. For a system exhibiting two phases, particle coarsening process obeys temporal power laws as shown in Eq. 1.4, Eq. 1.5 and Eq. 1.6. Much more details about derivation are given in Voorhees' work [30, 34]. Furthermore, Lifshitz and Slyozov [32] and Wagner [33] also predicted that particle size distribution is independent of initial conditions and self-similarly asymptotic.

$$\bar{R} \propto t^{\frac{1}{3}} \tag{1.4}$$

$$c_m \propto t^{-\frac{1}{3}} \tag{1.5}$$

$$N \propto t^{-1} \tag{1.6}$$

It is until LSW theory was developed that people had more interests on particle coarsening and started doing more studies on this process. Many experimental results of particle size distributions for a non-zero volume fraction system are border than that predicted in LSW theory. Since the predictions in LSW theory is based on the assumption that particles are source points, it implies that LSW theory is valid for a system of essentially zero volume fraction of second phase.

It is worth noting that the volume fraction of second phase is more than ten percent in many commercial alloys. As a consequence, volume fraction effect is of great importance. Various modifications of LSW theories of non-zero volume fraction cases have also appeared in the literatures. Ardell [35], Tsumuraya and Miyata [36] and Asimov [37] used diffusion geometry to elucidate the various factors which control particle coarsening kinetics including volume fraction, but failed to address the statistics of diffusional particle interactions properly. Brailsford and Wynblstt [38] originally suggested to use chemical rate theory and they successfully overcame the statistical averaging problem. Marqusee and Ross [20] approached the same problem using statistical method. Glicksman and Voorhees [39, 40] applied computer simulation to solve the diffusion control problem between multiple particles. Tokuyama and Kawasaki [41] viewed particle coarsening as a statistical mechanical model. These theories [38, 20, 39, 40, 41] lead to different results from the quantitative point of view, even though they all take into account the volume fraction of second phase.

1.1.4 Factors that influence particle coarsening

Speaking of factors affect particle coarsening rate and kinetics, it has generated a great deal of experimental interest since the revelation of Ostwald ripening.

Grewal et al. [42] studied the factors that influence the rate of particle coarsening in Ti-Mn alloy and Ti-V alloy, respectively. They claimed that, for the Ti-Mn system, matrix and grain boundaries play important roles at low temperature (973K), and it is only controlled by bulk diffusion when the temperature increases to 1108K. For Ti-V system, the rate-controlling factor for particle coarsening is grain boundary at 973K, then it tends to be controlled by matrix diffusion and grain boundary diffusion at 1073K. However, since they simply focused on the influences of matrix and grain boundaries, they failed to take into account the fact that diffusional interactions between second-phase-particles should not be ignored.

Gleiter et al. [43] and Bibbons et al. [44] have studied particle coarsening in nickel base alloys, respectively. Although there was no revelation of volume fraction effects in their experimental results, several studies [45, 46, 47, 48] have successfully completed. According to LSW theory [32, 33], the average particle size $\bar{r}$ is proportional to time t, which is shown in Eq. 1.7.

$$\bar{r}^3 - \bar{r}_0^3 = kt \tag{1.7}$$

where $\bar{r}_0$ is initial particle size, k is particle coarsening rate constant. As shown in Table 1.1, different k values corresponding to alloys with different volume fractions

Table 1.1: Particle-coarsening rate for various systems [45, 46, 47, 48]

Alloys	Temperature (K)	Volume Fraction	k(m^3 sec^{-1})
Ni-6.35Al	898	0.145	2.12×10^{-30}
Ni-6.71Al	898	0.198	2.00×10^{-30}
Ni-6.35Al	988	0.091	7.25×10^{-29}
Ni-6.71Al	988	0.148	6.77×10^{-29}
Ni-7Al	1073	0.090	1.10×10^{-27}
Ni-8Al	1073	0.270	1.06×10^{-27}
Ni-9Al	1073	0.440	1.20×10^{-27}
Ni-9.9Al	1073	0.600	1.30×10^{-27}
Ni-14.3Cr-4.4Al	1198	0.090	1.01×10^{-25}
Ni-13.5Cr-5.8Al	1198	0.420	1.70×10^{-25}
Ni-9.3Co-11.79Al	973	0.160	1.41×10^{-29}
Ni-9.5Co-12.60Al	973	0.240	1.79×10^{-29}
Ni-22.1Co-10.77Al	973	0.160	1.09×10^{-29}
Ni-21.7Co-13.40Al	973	0.310	1.11×10^{-29}

at the same temperatures prove that volume fraction is an important factor that influences particle coarsening rate.

In terms of particle motion, both LSW theory and its modifications assume that precipitates of second phase are fixed without movement in most alloys, which is an indication of being ignorant of particle motion. It is worthwhile to point out that experimental results show great difference in particle motion rate between solid precipitate-solid matrix systems and solid precipitate-liquid matrix systems. Courtney [49, 50] has studied the influence of particle motion in systems where solid particles are distributed in liquid matrix. More particle contact, due to Brownian motion, Stokes motion and convection currents, results into significant effect on particle coarsening rate. Correspondingly, Johnson et al. [51] calculated the velocity of particles in a solid matrix system. It turns out that particle motion is too slow to affect coarsening kinetics. From this perspective, it is reasonable for LSW theory and its modifications to assume little effect of particle motion in solid particle-solid matrix systems throughout particle coarsening process.

Jayanth and Nash [52] have reviewed several factors affecting particle-coarsening kinetics such as volume fraction of second phase, diffusion control of grain boundaries, diffusional interactions between precipitates, external stresses and irradiation. It is worth noting that factors including external stresses and irradiation could not be applied to most systems because these are external factors that only work for exceptional cases.

In general, there are four major factors which influence particle coarsening as follows: volume fraction of second phase, matrix diffusion, grain boundary diffusion, and diffusional interactions between particles.

1.2 Precipitation free zones

1.2.1 Influences of precipitation free zones on mechanical behaviours

Almost all age-hardening alloys exist regions or zones adjacent to grain boundaries which are depleted of precipitates. These regions are called Precipitate Free Zones (PFZs). As a common sense, PFZs exist in Al-based alloys, Mg-based alloys, Ti-based alloys, Fe-based alloys and Ni-based alloys. Figure 1.4 illustrates PFZs along grain boundaries. It clearly shows that there is no precipitate in the bright area along grain boundary (i.e., the grey line). Big precipitates at grain boundary and relatively small precipitates inside the grain could be seen as well. Since the performance of most polycrystalline materials is largely dependent on the microstructures, there have been lots of researches regarding PFZs in these alloys. However, the formation and growth mechanism of PFZs is still under intensive discussion.

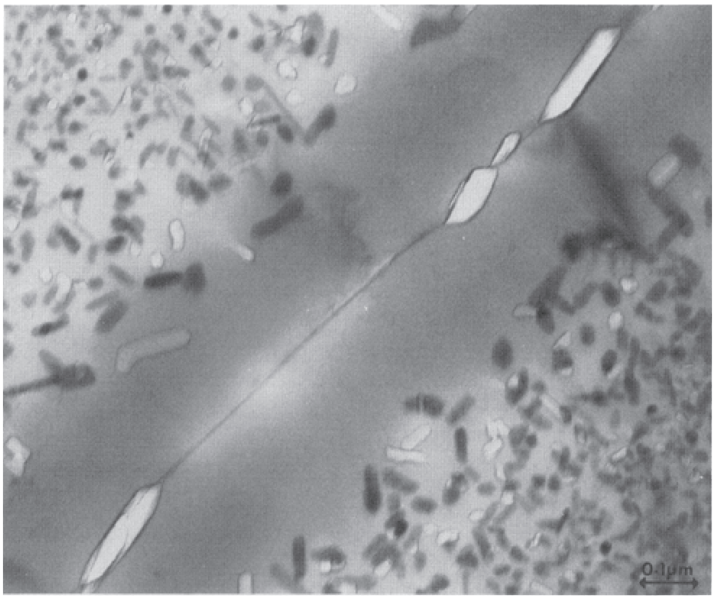

Figure 1.4: PFZs in Al-2.2 at. pct-4.7 at. pct Mg alloy [53]

In regards to the influence of PFZs on materials, researchers hold different viewpoints. Many studies have showed that the formation and growth of PFZs along the grain boundary significantly reduce mechanical performance of materials [54]. For instance, the preferential deformation of PFZs would result in micro cracks in PFZs [55]. Starink [56] pointed out that the overall impact of PFZs is that they reduced reinforcement of precipitate phase in the matrix.

There also has been a widespread discussion regarding how PFZ influences stress corrosion cracking (SCC) in aluminum alloys. A remarkable review was done by Starke et al [57]. To the best of knowledge, most of previous studies concentrated on attempting to correlate the PFZ width with SCC susceptibility. However, it appears more reasonable, as suggested by Doig and Edington [58], to correlate the SCC susceptibility with solute distribution in the PFZs. According to Ward and Lorimer [59], it is clearly demonstrated that, in Cu modified Al-Zn-Mg alloys, no Cu depletion is found in the PFZ, and SCC resistance is improved at the same time. Similar results have also been obtained, including [53] where copper is seen to distribute fairly uniformly across the PFZs in aluminum alloy AA7075. From this point of view, the microanalysis technique provides a better understanding of local solute distribution in the PFZs that affects the behavior of SCC in alloys.

For the welding alloys, the more heat is input by welding, the wider PFZ appears [60]. The existence of PFZs makes partial melted region easy to crack in the process of tension and impact in the intergranular fracture fashion.

PFZs also lower the yield strength of Ni-based alloys. As the width of PFZs increases, the reduction of yield strength becomes larger [61]. This is because when the width of PFZs exceeds a limit, there are plenty of cross-slips and double cross-slips in the PFZs. This leads to the creation of dislocation sources that emit dislocations. These dislocations pile up leading to the reduction of yield strength of alloys. Therefore, wide PFZs are undesirable because they adversely affect the mechanical behaviours, fracture resistance and stress corrosion cracking resistance of several alloys.

1.2.2 Formation of precipitation free zones

Generally speaking, there are two different kinds of theories explaining the formation mechanism of PFZs. One is referred to as the vacancy density theory, which is, for instance, supported by Jha et al [62] who claimed that PFZ is derived from vacancy consumption. The vacancy density in the solution of alloy is pretty high due to high temperature of heat treatment. However, the aging temperature is much lower. Many vacancies are generated when the alloy is fast quenched from high temperature. At the same time, grain boundaries would absorb vacancies due to the reason that the grain boundaries are the main trap of excess vacancies, and diffusion coefficient of vacancy is very high. As a consequence, the vacancy density along grain boundary is as low as that in the aging treatment, whereas the vacancy density inside grain is still as high as that in the solution heat treatment. Thus, there is a gradient of vacancy density perpendicular to grain boundary in the zone near the grain boundary. And as a common sense, it is hard for solute atoms to diffuse under the circumstance of low vacancy density. In this case, PFZs appear when the vacancy density along the grain boundary is lower than the threshold density required for the nucleation of second phase.

The other theory is the solute depletion theory, wherein Yao et al [63] proposed that desolvation of particles is faster at grain boundary than inside grains since grain boundaries consume solute atoms near the grain boundaries and enable PFZs to appear. To be more specific, concentration of solute atoms at grain boundaries is lower than that near grain boundaries. Thus the concentration gradient leads to flux of solute atoms towards grain boundaries. PFZs form gradually as all solute atoms of precipitates near grain boundaries flow to grain boundaries. In addition, some researchers [64, 65] also argued that the formation of PFZs is caused by solute depletion, which has also been proved by microstructural features such as expansion of PFZ width with increased aging time and so on.

Jata et al [60] studied the formation mechanism of PFZs through observation and microstructure examination of PFZs in the fusion zone on the surface of welding high-strength aluminum alloy. Their experimental results show that formation of PFZs is mainly caused by migration of solute phase along grain boundary. And the driving force is the coherent strain energy, strain energy difference caused by weld shrinkage and interface energy difference of grain boundary caused by the curvature.

There are some other researchers [66, 67, 68] stating that PFZ is formed by solute depletion mechanism at the early stage of aging treatment; after that, the formation of PFZ is governed by vacancy depletion mechanism. Based on these works [64, 65, 68], the solute depletion theory is preferred to explain the early stage of PFZs' formation.

1.2.3 Growth of precipitation free zones

No matter they are stable or metastable precipitates, their growth needs a large amount of solute atoms. Solute atoms play important roles in the nucleation of particles. Microstructural examinations show that the formation and growth of PFZs significantly depends on solute atoms. A lot of different explanations have been proposed about the change of PFZ width in aging treatment. In order to study the distribution of the solute atoms near the PFZs, researchers mainly adopted several microscopic analysis methods (such as X-ray analysis and three-dimensional atom probe (3DAP)) [55, 53, 69, 70]. X-ray analysis showed that concentration of solute atoms in the PFZs is smaller than that inside grains [69, 70]. 3DAP results showed that concentration of solute atoms in matrix remain the same with that in quenching state [53].

Ogura et al stated that PFZs would be wider with the increase of aging time under the same aging temperature [55]. However, Raghavan [53] argued that the width of the PFZs would not become wider as the aging time increases. His experimental measurements show that the width of PFZs is far more sensitive to the aging temperature than to the aging time, i.e., the higher the aging temperature is, the greater the width of PFZs will be. During conventional aging of alloys, decomposition of the solid solution involves one or more metastable phases because of the differences between solid solubilites of these phases. The formation of PFZs is expected to be seen in such cases. On the other hand, PFZs should not form or grow to any significant extent when decomposition directly results into the stable precipitate.

Classical diffusion theory as shown in Eq. 1.8 is often applied to explain the growth of PFZs [71, 72, 73] based on solute depletion theory.

$$D = D_0 exp(-\frac{Q}{RT}) \tag{1.8}$$

where D is diffusion coefficient, D_0 is maximum diffusion coefficient, Q is activation energy, R is gas constant and T is temperature. The diffusion of solute atoms leads to the formation of PFZs. As time t goes on, the width of PFZs x will be in a fashion as shown in Eq. 1.9.

$$x = 2\sqrt{Dt} \tag{1.9}$$

Some researchers even measure the PFZ width to calculate the diffusion coefficient using Eq. 1.9 [74], since they considered the diffusion distance is almost the same as PFZ width.

Ringer et al [68] obtained samples with different width of PFZs by different quenching methods and different aging treatments. Through observation by transmission electron microscopy, they found that the width of PFZs becomes narrower with the increase of quenching speed. They also found that the width of PFZs gradually becomes larger with the nucleation and growth of precipitates at grain boundary in the aging treatment.

Furthermore, the width of the PFZs is dependent on orientation difference of two adjacent grains and the types of grain boundaries. Experimental results showed that precipitates near the large angle grain boundaries are significantly greater than those near small-angle grain boundaries, which indicates two different structures of precipitates at grain boundaries. Precipitates on the small-angle grain boundaries are coherent with the matrix. As a result, matrix prevents these precipitates from growing rapidly. At the large angle grain boundaries, it mainly forms stable precipitates with big misfits with matrix, which means these precipitates are able to grow quickly, and thus absorb more solute atoms. In some alloys [75], diffusion rate of solute atoms at the large-angle grain boundaries is greater than that at the small-angle grain boundaries, which leads to wider PFZs at large-angle grain boundaries. In some superalloys, additional elements are introduced in order to reduce the capacity of grain boundaries to absorb solute atoms [76]. PFZs fail to form close to these types of grain boundaries.

1.3 Mean Field Method

Nowadays, considering the increasing needs of applications in the area of information sciences, scores of researchers are paying more attention to the study of large-scale and highly-coupled probabilistic systems as representative models in statistical physics. In these fields, Markov Chain Monte Carlo (MCMC) methods [77] and MFM [78] are playing particularly significant roles since they are two of the most widely-used approaches.

MCMC methods have largely sparked innovative applications throughout information sciences, due to its appealing generality and simplicity of implementation methods [79]. Since the roots lie in the simulation of gases and condensed matter, MCMC methods work in a sampling-based fashion [80, 81]. On the other hand, MFM, in most cases, can also solve the problems that are addressed by MCMC methods. As deterministic methods, however, MFM uses a different set of conceptual and mathematical tools, such as Taylor expansions and convex relaxations, to approximate and bound quantities of interest [82]. Therefore, it is seen that MFM is basically built up based upon the optimization theory and perturbation theory, while MCMC methods are generally supported by the theory of Markov chains and stochastic matrices.

Here it is nontrivial to point out that a major concern of modern probabilistic modeling is the huge computational complexity resulted from complicated calculations with multivariate probability distributions, especially when the number of random variables becomes pretty large. A case in point is that MCMC methods might reach their limits in probabilistic data models, which leads to failure of tackling such kinds of problems [83]. In contrast, MFM is able to cope with such models with practical simplification and approximation, so that the final solution can be accordingly derived. Under this circumstance, an effective field is used to act on each individual random variable, which successfully replaces the mutual influence among multiple random variables. It can be further formulated, in its simplest version, in a form of approximation of the true distribution by a factorizable one. As a consequence, a closed set of nonlinear equations is derived by variational optimization of these products, which can usually be solved in polynomial time, i.e., a period of time that grows polynomially in the number of variables [84].

A useful application of MFM is a general framework in the area of statistical physics and information sciences [85], which associates joint probability distributions with graphs. To be more explicit, local clusters of nodes on a given graph can be taken together to define families of joint probability distributions, which in turn generate probabilistic graphical models being graphs-directed or undirected-annotated with these functions. Generally speaking, graphical models consist of two parts. One is classical models of statistical physics instances of graphical models involving undirected graphs, the other is applied probabilistic models without obvious connections to physics [86]. In practice, there have been a range of examples including phylogenetic trees in genetics [87], diagnostic systems in medicine [88], unsupervised learning models in machine learning [89], and error-control codes in information theory [90]. Thanks to the availability of such a general framework, it is possible to come up with more intuitive ideas that can be effectively carried out in various fields.

Another application of MFM is to predict phase transitions in physics [91], which is defined as discontinuities in aggregate properties of a system under the scaling of one or more parameters associated with the system. As a matter of fact, the values of microscopic variables often attract most interest, followed by the macroscopic properties of the system.

In this dissertation, we focus on the application of MFM in phase transformation. Dimensionless variables will be employed for the derivation of particle-coarsening rate. The dimensionless radius term ρ_i for any given particle i is defined as Eq. 1.10.

$$\rho_i = \frac{R_i}{\Gamma} \tag{1.10}$$

where R_i is dimensional radius and Γ is capillary length. A dimensionless concentration term around any given particle Θ_i is defined as Eq. 1.11.

$$\Theta_i(t) = \frac{c_i(t) - c_e}{c_e} \tag{1.11}$$

where t is dimensional time, $c_i(t)$ is dimensional concentration around any given particle i and c_e is equilibrium concentration. Combining the linearized Gibbs-Thomson Eq. 1.2, Eq. 1.10 and Eq. 1.11 yields Eq. 1.12.

$$\Theta_i = \frac{1}{\rho_i} \tag{1.12}$$

And a dimensionless average concentration term for any specified domain Θ_m is defined as Eq. 1.13.

$$\Theta_m(t) = \frac{c_m(t) - c_e}{c_e} \tag{1.13}$$

where $c_m(t)$ is dimensional average concentration for any specified domain. A dimensionless time term τ is defined as Eq. 1.14.

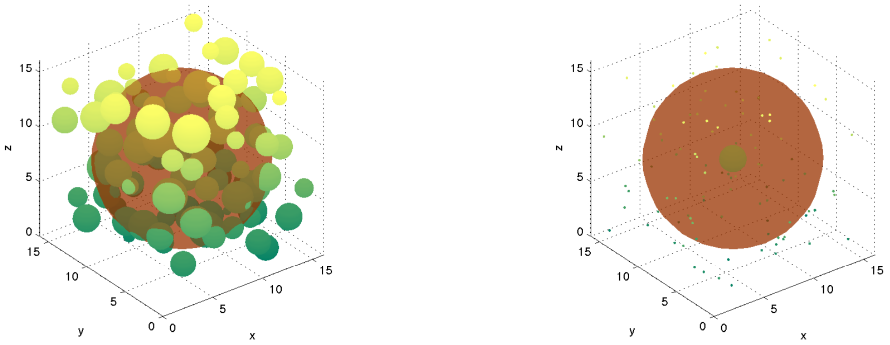

(a) (b)

Figure 1.5: Mean-field assumption. (a) illustrates a real situation that particles are randomly distributed, (b) describes an ideal model by mean-field assumption.

$$\tau = \frac{Dc_e}{\Gamma^2} t \tag{1.14}$$

where D is the diffusion coefficient.

As what has been addressed in Section 1.1, MFM has been employed in LSW theory. When dealing with a large number of coarsening particles, MFM helps to simplify the problem formulation based on one single equation rather than sloving multiple relevant equations. Thus, with the mean-field assumption, the center particle of any specified domain is treated as if it were independent of any other particle. Like what has been shown in Figure 1.5, the real case in Figure 1.5 (a) is transformed into Figure 1.5 (b) with the mean-field assumption. All other particles in shaded domain are considered as source points and merged into this specified area with an average concentration Θ_m. Assume the radius of this center particle is large enough to cover the whole background, which means R_i goes to infinity, then the boundary concentration of this center particle is the average concentration of its background as shown in Eq. 1.15 [92].

$$\Theta_i(R_i \to \infty) = \Theta_m(\tau) \tag{1.15}$$

MFM tremendously simplifies the diffusion problem in particle coarsening process based on two assumptions: a) equilibrium volume fraction of second phase is low enough to be negligible, and b) the average distance between any two particles is large enough so that particles can be treated independently. Under this circumstance, all other particles are treated together and solute flux toward any center particle are derived based on the term Θ_m, which could be kept tracking of. Notably, in the LSW theory, the effect of nucleation and particle coalescence is neglected, which means that the flux of the whole system is set to zero [32, 33]. Hereafter, the diffusion field in the matrix is governed by Eq. 1.16.

$$\bigtriangledown^2 \Theta_i(\tau) = 0 \tag{1.16}$$

along with the boundary conditions Eq. 1.12 and Eq. 1.15 leads to the growth rate of any particle in Eq. 1.17.

$$\frac{d\rho_i}{d\tau} = \frac{1}{\rho_i}(\Theta_m(\tau) - \frac{1}{\rho_i}) \tag{1.17}$$

It is worthwhile to point out here that Eq. 1.17 captures the essential features of particle coarsening process. From Eq. 1.17, there is a critical size ρ_c for particles,

$$\rho_c(\tau) = \frac{1}{\Theta_m(\tau)} \tag{1.18}$$

And particles of critical size should neither shrink nor grow since

$$\frac{d\rho_i(\rho_i = \rho_c)}{d\tau} = 0 \tag{1.19}$$

Intuitively, particles with a radius that is larger than ρ_c should grow and vice versa, since

$$\frac{d\rho_i(\rho_i > \rho_c)}{d\tau} > 0 \tag{1.20}$$

$$\frac{d\rho_i(\rho_i < \rho_c)}{d\tau} < 0 \tag{1.21}$$

From what has been derivated, we can see that large particles tend to grow and small particles should shrink or even dissolve, which agrees well with what has been discussed in Section 1.1.

1.4 Boundary Element Method

BEM is a useful approach of obtaining solutions to integral equations. It is used to derive boundary integral equations, in particular when integral equations on the boundary of the physical domain are transformed from elliptic boundary value problems on spatial domains. In recent decades, BEM has been developed to be a useful tool of numerics. Some notable well-developed techniques include BEM for modeling viscous flow and free surface flows [93], simulation of cavitatin, BEM for geometrically nonlinear analysis of plates and shells [94], modeling of plates and shells by meshless local BEM, fast hierarchical BEM for large scale 3D elastic problems, time domain BEM techniques [95], Greens function evaluation for three dimensional exponentially graded elasticity and BEM for the fracture analysis of the general piezoelectric solids [96].

Furthermore, because BEM has become applicable to a considerable number of engineering problems in a wide range of fields [97, 98], BEM keeps attracting increasing attention. A case in point is the problem of heat transfer [99], which is effectively addressed by BEM. In practical scenarios such as linear and non-linear steady-state heat conduction, lots of problems like thermal radiation can be formulated in a simple and elegant fashion thanks to BEM as well. On the other hand, some heat transfer problems lead to an integral equation with domain integrals, which cut down the efficiency of the method and further make it far more difficult to prepare data for coding on computers. As a remarkable milestone, related methods were developed to transform integrals into boundary ones with the help of BEM [100]. Most effectively, the reciprocity theorem is widely used, which has been proved to be capable of achieving good performance in efficiency as well as accuracy in many numerical experiments. Generally speaking, there exist two different ways of accomplishing the transformation including dual reciprocity method [101, 102, 103] and multiple reciprocity method [104, 105].

This section addresses a classical multiparticle diffusion problem using boundary element formulation. In the sense that an equivalent boundary integral equation is derived from the proper fundamental solution to the diffusion equation, such kinds of formulation can be viewed as a direct extension of potential theory. In literature, Morse et al. [106] and Carslaw et al. [107] adopted free-space Greens function to obtain analytical solutions to several simple problems. Chang et al. [108] and Shaw [109] applied this fundamental solution in the context of direct BEM for the first time, even though the analytical aspects of the method instead of the numerical parts were emphasized. The formulation was then extended by Wrobel et al. [110], which included space and time interpolation functions in higher order, and thereafter successfully analyzed practical engineering problems.

One of the shortcomings of LSW theory is that it is based on the assumption of zero volume fraction, which inevitably ignores the diffusional interaction between particles. With the center particle being no longer independent, it is essential to determine the diffusional distance of a particle of a given size, which is statistically averaged with its surroundings. Because BEM takes part of the neglected correlations between random variables into consideration, it is a useful approach to deal with such cases. Its formulation can be viewed as a direct extension based on potential theory in that the proper fundamental solution to the diffusion equation is used to derive an equivalent boundary integral equation.

Therefore, the diffusion problem here is formulated in an integral form, which spontaneously covers the boundary conditions. According to Poissions equation and Dirac delta function, the surface of every single particle is integrated to a certain integration point from each field point, and further ends up with homogeneous Fredholm integral equation of the second kind with Gibbs-Thomson boundary conditon. The solution gives out a single layer density yielding a constant concentration on the surface of each particle. In terms of BEM, the integral equation can be then simplified to a set of linear equations, and all of the coefficients of the spherical harmonics can be settled once a term is determined [111]. Here it gives Eq. 1.22 based on Θ_m which is the specified concentration term.

$$\frac{1}{\rho_i} = \Theta_m(\tau) - \rho_i \frac{d\rho_i}{d\tau} - \sum_{j \neq i}^{N} \frac{\rho_j^2 \frac{d\rho_j}{d\tau}}{\mid \vec{r_i} - \vec{r_j} \mid} \tag{1.22}$$

where $\mid \vec{r_i} - \vec{r_j} \mid$ is the distance from center of particle i to center of particle j. The growth rate of any particle could be derived as shown in Eq. 1.23 by simply transforming Eq. 1.22.

$$\frac{d\rho_i}{d\tau} = \frac{1}{\rho_i}[\Theta_m(\tau) - \frac{1}{\rho_i}] - \frac{1}{\rho_i} \sum_{j \neq i}^{N} \frac{\rho_j^2 \frac{d\rho_j}{d\tau}}{\mid \vec{r_i} - \vec{r_j} \mid} \tag{1.23}$$

Here we could compare Eq. 1.17 and Eq. 1.23 which are both growth rate of any particle. Eq. 1.23 is derived using BEM while Eq. 1.17 is generated from MFM. Apparently, there is an additional part in Eq. 1.23 than in Eq. 1.17. In particular, this part represents the solute flux B_j from any particle j to the matrix as shown in Eq. 1.24.

$$B_j = \rho_j^2 \frac{d\rho_j}{d\tau} \tag{1.24}$$

This part reveals how the center particle i is influenced by other particles that are located in a sphere with a radius determined by the cutoff distance, i.e., the statistical average diffusional distance. For instance, the growth of the center particle i is accelerated by a positive flux from matrix to particle i in that particle i is able to take solute atoms. And the growth of the center particle i is prevented by a positive flux from matrix to particle j in that particle j is able to take solute atoms. It is also worth noting that the center particle i gets greater influence from particle j if they are closer to each other in distance. Apparently it captures the fundamental features of multiple particle coarsening.

1.5 Objectives and outlines

On this line, this work investigates a more rigorous description of the diffusion process valid for particle coarsening and PFZ growth. In order to derive an expression for the growth rate of particles, MFM and BEM are taken into account, which solve the diffusion equation in three dimensions. Further, such an expression in turn predicts a kinetic expression for the PFZ growth rate.

The structure of this thesis is as follows. A brief summary of the relevant concepts and research in particle coarsening and PFZs is presented in Chapter 1. It also gives the background of particle coarsening problem solved by MFM and BEM. Chapter 2 summarizes the method in a way that is useful for studying particle coarsening and PFZs. It describes the mathematics that goes into the computer implementation of particle coarsening process as well. Chapter 3 shows simulation results for verifying the proposed model. It also contains a discussion of the implication of the results. Chapter 4 gives the conclusions and Chapter 5 shows future directions of research.

Chapter 2

Mathematical methods and simulations

2.1 Particle coarsening far away from grain boundaries

When it refers to particle coarsening inside the grains and far away from grain boundaries, the total solute flux in the system equals to zero. It is no longer necessary to consider the effect of grain boundaries. In other words, the total solute flux in the system is equal to zero. We also assume that there is no nucleation or particle coalescence during particle coarsening process. Based on solute atoms conservation, the total number of solute atoms in the matrix together with the total number of solute atoms in the particles should be equal to the total number of solute atoms in the original system at any time as shown as Eq. 2.1.

$$c_0 = c_m(t) + \frac{4\pi}{3\nu}\int_0^\infty R^3 n(R,t)dR \tag{2.1}$$

where c_0 is the initial concentration in the matrix, $c_m(t)$ is the concentration in the matrix at time t, ν is molar volume, $n(R,t)$ is the number of particles of size R per unit volume at time t. It is worthwhile to scale radius R, concentration c and time t to dimensionless radius ρ, concentration Θ and time τ using Eq. 1.10, Eq. 1.13 and Eq. 1.14. Then Eq. 2.1 could be rewritten as Eq. 2.2.

$$\Theta_m(\tau) = \Theta_0 - \frac{4\pi\Gamma^3}{3\nu c_e}\int_0^\infty \rho^3 f(\rho,\tau)d\rho \tag{2.2}$$

where $f(\rho,\tau)$ is scaled dimensionless size distribution. Since capillary length Γ, molar volume ν and equilibrium concentration c_e are all constants, Eq. 2.2 could be rearranged as Eq. 2.4 using Eq. 2.3.

$$\alpha = \frac{4\pi\Gamma^3}{3\nu c_e} \tag{2.3}$$

where α is a constant, which could be calculated for a given system.

$$\Theta_m(\tau) = \Theta_0 - \alpha\sum_{i=1}^{N}\rho_i^3 \tag{2.4}$$

Thus, particle growth rate shown in Eq. 1.23 could be rewritten as Eq. 2.5.

$$\frac{d\rho_i}{d\tau} = \frac{1}{\rho_i}(\Theta_0 - \alpha\sum_{i=1}^{N}\rho_i^3 - \frac{1}{\rho_i}) - \frac{1}{\rho_i}\sum_{j\neq i}^{N}\frac{\rho_j^2\frac{d\rho_j}{d\tau}}{\mid \vec{r_i} - \vec{r_j} \mid} \tag{2.5}$$

Up until now, the growth rate of any given particle i at any given time τ could be calculated by taking advantage of iteration as long as α is known. It is worthwhile to point out here that the initial state is known for a given system, thus α could be calculated. From this perspective, we can keep track of particle coarsening process far away from grain boundaries with the help of MFM and BEM.

We employ 2,000 particles that are randomly distributed in a cubic system without overlapping. The particle size complies with a normal distribution $\mathcal{N}(1.0, 0.25)$, and the particle radius ρ is randomly chosen between 0.0001 and 2.0. The initial matrix concentration c_m and equilibrium concentration c_e are set to 0.1 and 0.05, respectively. The side length of this cubic system shown in Figure 2.1 (a) is calculated based on the volume fraction of components. In addition, periodical boundary conditions are applied in three dimensions.

The cutoff distance is derived according to solute depletion theory. As a consequence, each particle could have interactions only with particles that are within its cutoff distance. It should be noted, since the cutoff distance is likely to get larger due to diffusion, its value needs to be carefully chosen such that it keeps smaller than half of the system side length all the time. The initial cutoff distance set to 5 times the average particle radius.

The time step $d\tau$ is set to 0.01 times the cube of average particle radius on the basis of two conditions: a) the average value of particle radius is expected to be proportional to time according to LSW theory, and b) no more than one particle disappears after each time step.

The growth rate of each particle is therefore calculated using Eq. 1.23. The particle volume is updated and recorded after each time step. Particles with a radius smaller than 0.001 times the average radius being removed from the system. This procedure is repeated until 100 particles are left. The system is simulated with volume fraction

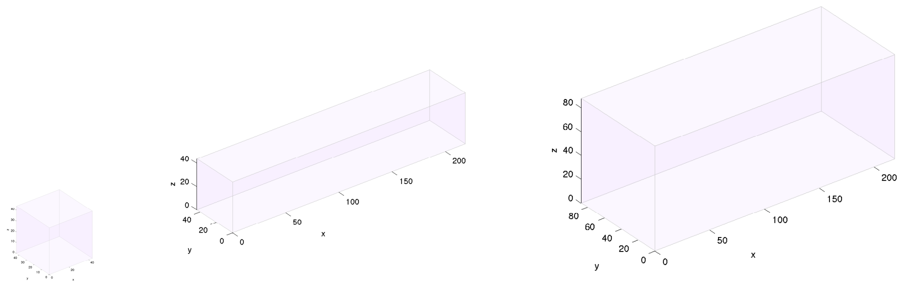

(a) (b) (c)

Figure 2.1: System size. (a) is a cubic system for 2,000 particles, (b) is a rectangular system for 10,000 particles, (c) is a rectangular system for 40,000 particles. All volume fractions are set to be 0.1 for these systems.

being 0.1.

2.2 Particle coarsening near grain boundaries

If particle coarsening happens near grain boundaries, it is necessary to consider the influence of grain boundaries. Based on the solute depletion theory, solute flux could be absorbed by grain boundaries. In other words, there is no solute atoms conservation. Since solute atoms near grain boundaries could be absorbed by grain boundaries more readily than those far away from grain boundaries due to time dependent diffusion, matrix concentration Θ_m is not homogeneous any more. At the same time, matrix concentration Θ_m is not only a function of time, but also a function of position, which could be represented by $\Theta_m(x, \tau)$, where x is the distance along side of system perpendicular to grain-boundary area. Thus, the particle growth rate in Eq. 1.23 could be rewritten as Eq. 2.6.

$$\frac{d\rho_i}{d\tau} = \frac{1}{\rho_i}(\Theta_m(x,\tau) - \frac{1}{\rho_i}) - \frac{1}{\rho_i}\sum_{j\neq i}^{N}\frac{\rho_j^2\frac{d\rho_j}{d\tau}}{\mid \vec{r_i} - \vec{r_j} \mid} \tag{2.6}$$

Concentration profile is shown in Figure 2.2. In this case, the system represents one grain between two paralleled grain boundaries with a large number of particles in it. As it was illustrated in Figure 2.2 at any given time τ, matrix concentration is position dependent. Grain boundary acts like a *sink* and there is a flow of solute atoms toward the grain boundaries. Solving Fick's second law under steady state concentration $\nabla^2\Theta_m(x) = 0$ with the boundary condition of zero concentration of solute atoms at the grain boundary results in a linear dependance of concentration from inside the grain toward the grain boundary. This linear relationship ends up at position x_1 where grain boundaries do not leave any influence on particles farther away than this distance. Thus, particles in the middle area could be treated without the consideration of grain boundaries as in Section 3.1, and matrix concentration maintains constant in the corresponding region. Additionally, Figure 2.2 shows the change of matrix concentration from time τ_1 to time τ_2. As time goes on, the slope appears to be more gentle, since the flux that goes to grain boundaries becomes smaller.

In order to calculate the particle growth rate near grain boundaries, we need to solve Eq. 2.6 based on the new definition of concentration term $\Theta_m(x, \tau)$. Therefore, it is necessary to illustrate the concentration profile in a rigorous way. Obviously, the concentration profile could be clearly defined as long as the constant value of Θ_m and the turning point position x are known. Θ_m could be calculated using Eq. 2.4 since it is position independent. If $dx/d\tau$ is known, then x could be calculated as well by taking advantage of iteration. It turns out that $dx/d\tau$ could be derived based on solute atoms conservation as shown in Eq. 2.7 and Fick's first law.

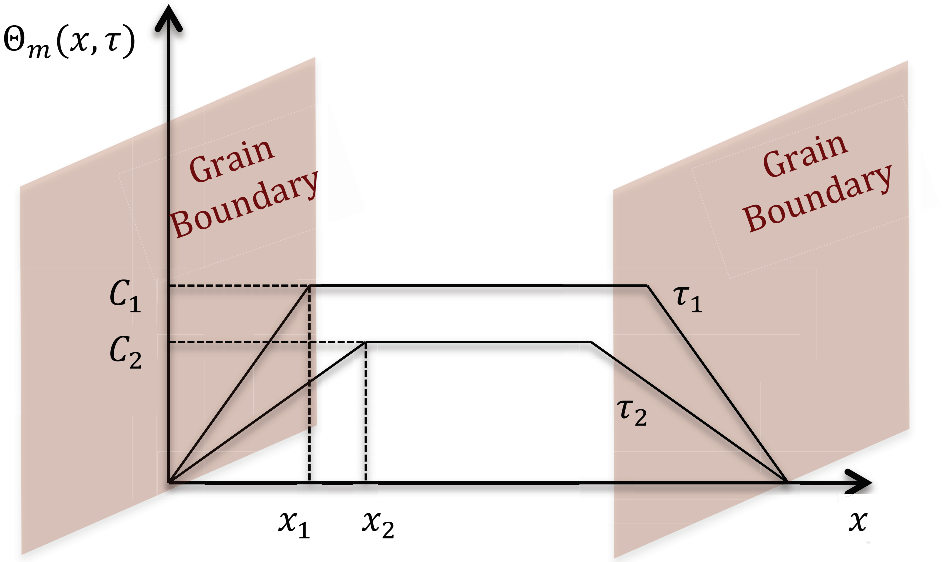

Figure 2.2: Concentration profile between two paralleled grain boundaries

$$N = cV \tag{2.7}$$

where c is concentration, N is the total number of solute atoms in the system and V is total volume of the system. And N could be rewritten in Eq. 2.8 since solute atoms exist either in matrix phase or in particles.

$$N = c_m V_m + c_p V_p \tag{2.8}$$

where c_m is matrix concentration, V_m is the total volume of matrix, c_p is particle concentration and V_p is the total volume of all particles. Thus V_p is the summation of each particle as shown in Eq. 2.9.

$$V_p = \frac{4}{3}\pi \sum_i R_i^3 \tag{2.9}$$

where R_i is the particle radius of any given particle. For V_m, we could refer to concentration profile in Figure 2.2. Apparently, covered area represents the total volume of matrix. Thus, V_m could be written in a way as shown in Eq. 2.10.

$$V_m = A(L - 2x) + \frac{1}{2}Ax + \frac{1}{2}Ax \tag{2.10}$$

where A is the area of grain boundary, L is the side length of the system which is perpendicular to grain boundary area and x is the position of turning point in the concentration profile. Hence, the total number of solute atoms could be rearranged as shown in Eq. 2.11.

$$N = c_m A(L - x) + c_p(\frac{4}{3}\pi \sum_i R_i^3) \tag{2.11}$$

Since both x and R_i are functions of time, the rate of change of N could be written in Eq. 2.12.

$$\frac{dN}{dt} = \frac{d}{dt}[c_m A(L - x)] + c_p 4\pi \sum_i R_i^2 \frac{dR_i}{dt} \tag{2.12}$$

On the other hand, the rate of change of total solute atoms must be equal to number of solute atoms in or out of the system per unit time across the grain boundary area. In this sense, the rate of change of N could be written in Eq. 2.13.

$$\frac{dN}{dt} = 2AJ \tag{2.13}$$

where J is the flux towards grain boundary. It is worthwhile to point out there will be double flux because there are two paralleled grain boundaries in the system. Then we will have an equation as shown in Eq. 2.14.

$$2AJ = \frac{d}{dt}[c_m A(L-x)] + c_p 4\pi \sum_i R_i^2 \frac{dR_i}{dt} \tag{2.14}$$

We assume that atom fraction in particles is 1, thus the concentration of particles c_p could be rewritten in Eq. 2.15.

$$c_p = \frac{1}{\nu} \tag{2.15}$$

where ν is atomic volume.By dividing Eq. 2.14 with $V = AL$ on both sides, we could get Eq. 2.16.

$$2\frac{J}{L} = \frac{d}{dt}[\frac{c_m(L-x)}{L}] + \frac{4\pi}{V\nu} \sum_i R_i^2 \frac{dR_i}{dt} \tag{2.16}$$

Then Fick's First Law could be scaled from Eq. 2.17 to Eq. 2.18 using Eq. 1.13.

$$J = -D \bigtriangledown c \tag{2.17}$$

$$J = -Dc_e \bigtriangledown \Theta \tag{2.18}$$

From Eq. 1.13, we can also get differential form of concentration term as shown in Eq. 2.19. At the same time, the first part of Eq. 2.16 could be rewritten in Eq. 2.20 and Eq. 2.21.

$$\frac{dc_m}{dt} = c_e \frac{d\Theta_m}{dt} \tag{2.19}$$

$$\frac{d}{dt}[c_m(1-\frac{x}{L})] = (1-\frac{x}{L})\frac{dc_m}{dt} - \frac{c_m}{L}\frac{dx}{dt} \tag{2.20}$$

$$\frac{d}{dt}[c_m(1-\frac{x}{L})] = (1-\frac{x}{L})\frac{dc_m}{dt} - \frac{[(c_m-c_e)+c_e]}{c_e}\frac{c_e}{L}\frac{dx}{dt} \tag{2.21}$$

Combine Eq. 2.18, Eq. 2.19 with Eq. 2.21, and we will have Eq. 2.22.

$$-2\frac{Dc_e}{L}\bigtriangledown\Theta = c_e\frac{d\Theta_m}{dt}(1-\frac{x}{L}) - \frac{c_e\Theta_m}{L}\frac{dx}{dt} - \frac{c_e}{L}\frac{dx}{dt} + \frac{4\pi}{V\nu}\sum_i R_i^2\frac{dR_i}{dt} \tag{2.22}$$

Eq. 2.22 could be rearranged in a more clear way as shown in Eq. 2.23.

$$-2\frac{Dc_e}{L}\bigtriangledown\Theta = c_e(1-\frac{x}{L})\frac{d\Theta_m}{dt} - (\Theta_m+1)\frac{c_e}{L}\frac{dx}{dt} + \frac{4\pi}{V\nu}\sum_i R_i^2\frac{dR_i}{dt} \tag{2.23}$$

Notably, the relationship between concentration and position is like Eq. 2.24 based on concentration profile in Figure 2.2.

$$\bigtriangledown\Theta = \frac{\Theta}{x} \tag{2.24}$$

Furthermore, it is of great benefit to scale length x and time t in Eq. 2.23 with the help of Eq. 1.10 and Eq. 1.14. In order to make it easy to be observed in the concentration profile, x is still used in the following equations but it is a dimensionless length term in the rest of this chapter.

$$-2\frac{Dc_e}{L\Gamma^2}\frac{\Theta_m}{x}=c_e\frac{d\Theta_m}{d\tau}\frac{Dc_e}{\Gamma^2}(1-\frac{x}{L})-\frac{Dc_e^2}{L}(\Theta_m+1)\frac{\Gamma}{\Gamma^3}\frac{dx}{d\tau}+\frac{4\pi}{V\nu}\frac{Dc_e\Gamma^3}{\Gamma^2}\sum_i\rho_i^2\frac{d\rho_i}{d\tau} \quad (2.25)$$

We could get Eq. 2.26 by arranging Eq. 2.25.

$$\frac{dx}{d\tau}=\frac{(1-\frac{x}{L})\frac{d\Theta_m}{d\tau}+\frac{2\Theta_m}{c_exL}+\frac{4\pi\Gamma^3}{V\nu c_e}\sum_i\rho_i^2\frac{d\rho_i}{d\tau}}{\frac{\Theta_m+1}{L}} \quad (2.26)$$

Since capillary length Γ, molar volume ν, total volume of the system V and equilibrium concentration c_e are all constants for a given system, Eq. 2.26 could be rearranged as Eq. 2.28 using Eq. 2.27.

$$\beta=\frac{4\pi\Gamma^3}{V\nu c_e} \quad (2.27)$$

where β is a constant, which could be calculated for a given system.

$$\frac{dx}{d\tau}=\frac{(1-\frac{x}{L})\frac{d\Theta_m}{d\tau}+\frac{2\Theta_m}{c_exL}+\beta\sum_i\rho_i^2\frac{d\rho_i}{d\tau}}{\frac{\Theta_m+1}{L}} \quad (2.28)$$

So far, $dx/d\tau$ could be gained, and at the same time, $\Theta_m(x,\tau)$ is known. Therefore, for any given particle i near grain boundaries at any given time τ, its growth rate could be calculated by Eq. 2.6.

We would like to simulate particle coarsening inside a grain between two paralleled grain boundaries. And we employ 10,000 particles that are randomly distributed in a rectangular system without overlapping each other at the beginning of the simulations. It is seen that the number of particles is five times more than that in the previous simulations. In order to get a valid comparison with previous simulations, we consider that the system is five times bigger than the previous cubic system. As shown in Figure 2.1 (b), its shape could be considered as five cubic system distributed along the longest side of the rectangular system.

We also employ 40,000 particles in another rectangular system. The volume of this system is four times larger than the system consisting of 10,000 particles. Its shape is shown in Figure 2.1 (c) could be considered as four permeable rectangular system distributed perpendicular to grain boundaries.

Periodical boundary conditions are applied as well but only in two dimensions. To be more explicit, the system box is repeated periodically in y and z directions since two paralleled grain boundaries are perpendicular to x direction.

The growth rate of each particle is calculated using Eq. 2.6 and Eq. 2.28. The particle volume is updated and recorded after each time step. Similarly, the system is simulated with different volume fractions being 0.05, 0.1 and 0.2, respectively.

Chapter 3

Results and discussion

3.1 Particle coarsening far away from grain boundaries

3.1.1 Results of particle coarsening far away from grain boundaries

In this section, results of the particle coarsening process are presented. Figure 3.1 shows the case where 2,000 particles coarsen inside a grain. Grain boundaries do not show up since this zone is far away from grain boundaries. Figure 3.1 (a) is the initial state of the system. Different colors of particles represent the height of particles in three dimensions. 2,000 particles are distributed in this zone without overlapping. And no distinctive difference of particle size could be told. Figure 3.1 (b) does not have so much difference from Figure 3.1 (a) since it is still at the beginning of coarsening process. Figure 3.1 (b), Figure 3.1 (c) and Figure 3.1 (d) show a trend

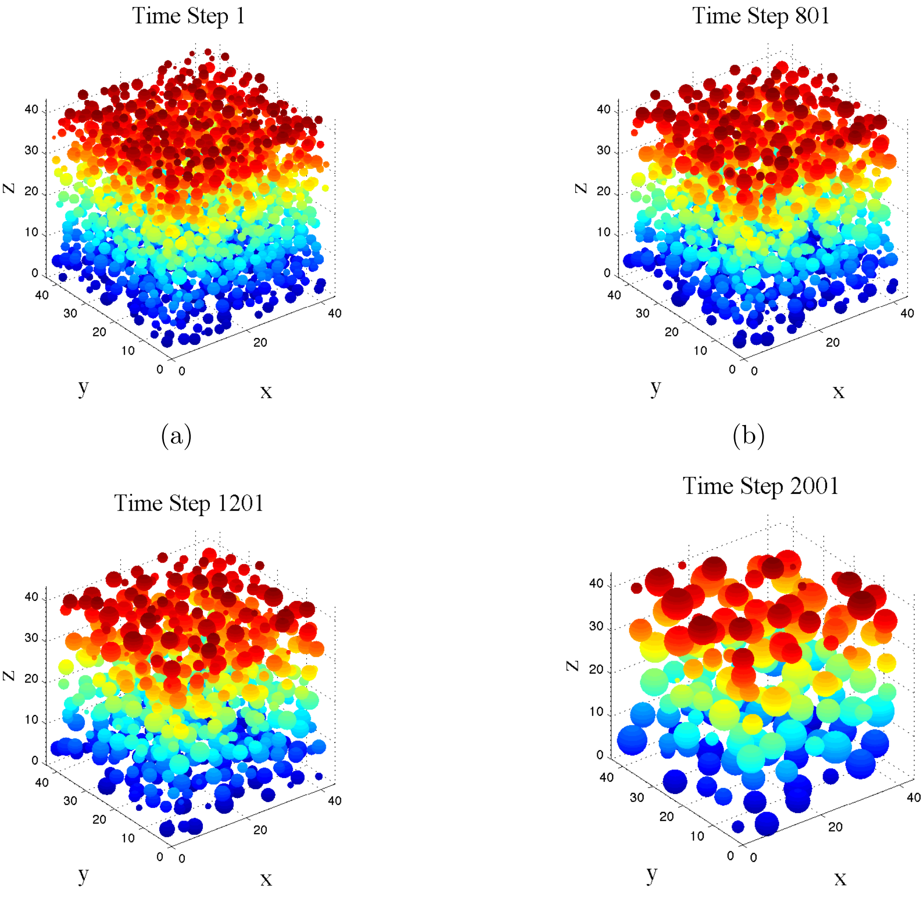

(a) (b)

(c) (d)

Figure 3.1: Particle coarsening far away from grain boundaries. 2,000 particles are initially randomly distributed in the system. (a), (b), (c), (d) illustrate the situations that are after time step 1, 801, 1201 and 2001.

that larger particles grow while smaller particles shrink. It is worthwhile to point out that particles do not overlap with each other during this process. In Figure 3.1 (d), it is obvious that some particles even disappear compared with Figure 3.1 (a).

Figure 3.1 captures the features of particle coarsening process. Like what happens in Ostwald ripening process, there is a flux from the small particles toward the large particles as a result of Gibbs-Thomson effect. Therefore, relatively larger particles grow and small particles in grains shrink and even disappear eventually. In addition, no overlapping could be found in the system, which accords with the experimental observations [112, 113]. From this point of view, the simulation results are consistent with particle coarsening process in practice. Therefore, the mathematical model based on MFM and BEM works for simulation of particle coarsening in grains of certain alloys.

Figure 3.1 reinterprets Figure 3.2 from the horizontal view. Figure 3.2 (a) shows the initial state where particle size follows the normal distribution. All the particles are inside the system. The trend of particle coarsening could be seen more clearly from Figure 3.2 (b) to Figure 3.2 (c). In Figure 3.2 (d), we can see that certain particles reach and even pass the boundaries of the system due to particle growing. The result does make sense since Mean-Field model only focuses on a zone inside one grain as a system. There is no real boundaries of this system. Meanwhile, introducing periodical boundary conditions in three dimensions indicates no boundaries of the system.

The other effect of periodic boundary condition is that a distinctive depletion is not observed in any part of the system and PFZs could not form even at the edge of system in all the images of Figure 3.2, which agrees with the features of experimental results [112, 114]. According to solute depletion theory [43], certain area or structure

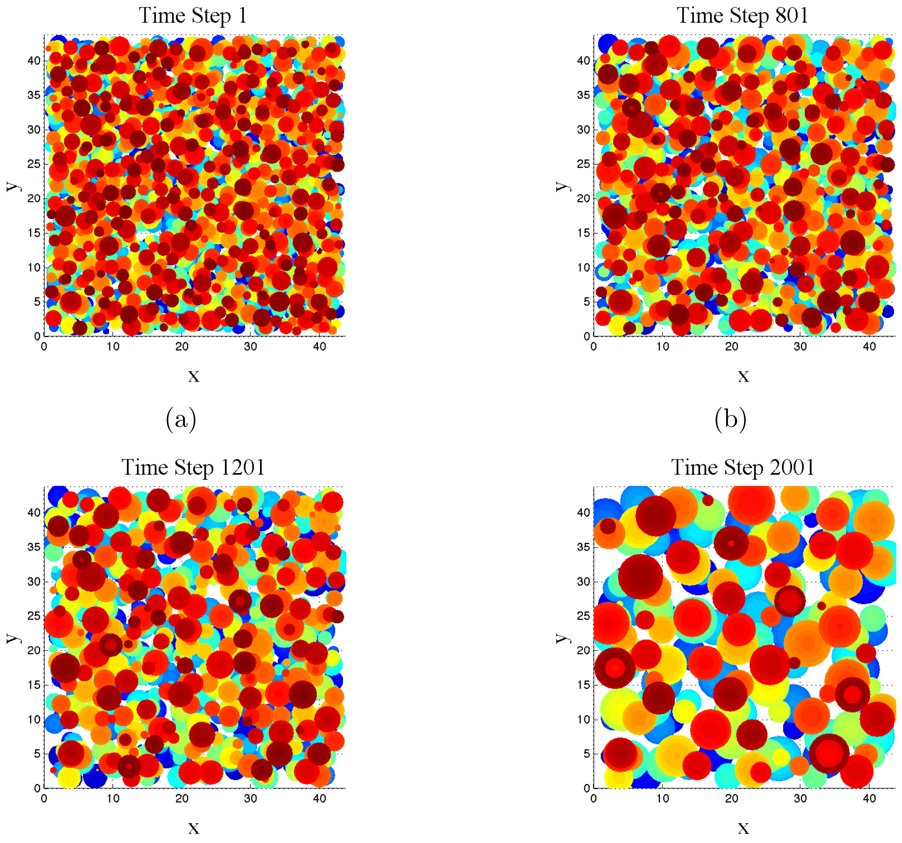

(a) (b)

(c) (d)

Figure 3.2: Horizontal view of particle coarsening far away from grain boundaries. 2,000 particles are initially distributed in the system without overlapping. (a), (b), (c), (d) illustrate the situations that are after time step 1, 801, 1201 and 2001.

consumes solute atoms of both matrix and particles, which leads to the formation of PFZs. Since this simulation focuses on a zone inside one grain composing of two phases, there is no other structures except for matrix and particles. Thus, solute atoms could not be absorbed, and PFZs will not form. These results assure us about the appropriate prediction of the model of the coarsening phenomenon in absence of a defect in the system.

3.1.2 Factors that influence the growth rate of particles far away from grain boundaries

As it was pointed out in Chapter 2, this model mainly embodies the influence of three factors on the growth rate of particles: a) volume fraction of second phase, b) matrix diffusion, and c) diffusional interactions between particles.

Firstly, the initialization of simulation reflects the influence of volume fraction of second phase. Based on MFM, the growth rate of particles that are far away from grain boundaries could be mathematically represented by Eq. 1.17. For a certain particle i with radius ρ_i, there are two terms based on volume fraction of second phase determining its growth rate $\frac{d\rho_i}{d\tau}$, which are the particles radius ρ_i and matrix concentration $\Theta_m(\tau)$. In terms of the influence of particle radius ρ_i on its growth rate, there is a critical size $\rho_c = 1/\Theta_m(\tau)$. The growth rate of a particle with radius ρ_i larger than ρ_c is positive while that smaller than ρ_c is negative. Therefore, particle-coarsening theory could be rephrased in a way that, particles with their size smaller than the critical size will shrink, while particles with their size larger than the critical size will grow. It is worth noting that ρ_c changes with time since matrix concentration $\Theta_m(\tau)$ is time dependent. Regarding another term matrix concentration $\Theta_m(\tau)$, it depends on initial matrix concentration Θ_0 during the whole simulation process, while Θ_0 is determined by volume fraction of second phase.

Secondly, the influence of matrix diffusion could be represented by matrix concentration $\Theta_m(\tau)$ in both Eq. 1.17 and Eq. 1.23. Matrix concentration plays a significant role in particle-coarsening process. The concentration gradient between the bulk matrix and the matrix around certain particles leads to flux of solute atoms. In addition, the directions and scales of flux to a particle determine whether this particle will grow or shrink , as well as the changing rate of its radius.

Last but not the least, diffusional interactions between particles also play an important role on the growth rate of particles. Its physical meaning is based on atom flux as well. According to BEM, compared with Eq. 1.17, there is an extra term in Eq. 1.23, which denotes as $\frac{1}{\rho_i}\sum_{j\neq i}^{N}\frac{\rho_j^2\frac{d\rho_j}{d\tau}}{|\vec{r_i}-\vec{r_j}|}$. This part reflects the influence of particle interactions. Additionally, there is a time dependent cutoff distance. Particles inside a virtual zone with the radius of cutoff distance will have influence on the center particle. In this sense, in Eq. 1.23, center particle i has interactions only with another particle j if their distance $\mid \vec{r_i} - \vec{r_j} \mid$ is shorter than the cutoff distance. Solute atoms from some particles inside the zone flow to the center particle, while solute atoms from the center particle flow to some other particles inside the zone. If the summation of solute atoms gained by center particle is positive during particle interactions, this center particle tends to grow, and vice versa. Since $\frac{1}{\rho_i}\sum_{j\neq i}^{N}\frac{\rho_j^2\frac{d\rho_j}{d\tau}}{|\vec{r_i}-\vec{r_j}|}$ is subtracted in Eq. 1.23, growth rate of the center particle will decrease if there is a positive flux of solute atoms $\rho_j^2\frac{d\rho_j}{d\tau}$ from the center particle.

3.2 Particle coarsening near grain boundaries

3.2.1 Results of particle coarsening near grain boundaries

Figure 3.3 shows coarsening phenomenon of 10,000 particles inside a grain located between two paralleled grain boundaries. In order to observe the process of particle coarsening, the horizontal view of the system is presented. There are two paralleled grain boundaries on the $y-z$ plane perpendicular to the x directions. Their location is calculated based on system size and initialization of shape located at $x = 0$ and $x = 218.78$, respectively. Different colors of particles represent the height of particle in three dimensions, which is also beneficial to differentiate particles in two dimensions since particles are overlapped with each other from horizontal view.

Figure 3.3 (a) shows the initial state of the system where 10,000 particles are distributed without overlapping each other. The particle size also follows the normal distribution. From Figure 3.3 (b) to Figure 3.3 (c), the fact that particle coarsening occurs is observable. These images show a trend that small particles shrink and even disappear while large particles grow. At the same time, PFZs form near two grain boundaries. There is hardly any particles left in these two zones at the vicinity of the grain boundaries. PFZs become wider as time goes on, which agrees with the experimental results [55, 115]. From this perspective, the mathematical model based on solute atoms conservation and diffusion theory achieves a good performance in simulating particle coarsening.

Figure 3.4 is the concentration profile of matrix along x direction that matches the system in Figure 3.3. The matrix concentration is homogeneous initially at time step 1 except for the areas near the grain boundaries. Instead, the concentration at grain boundaries is 0, which follows the mathematical model. It is an ideal assumption that solute atoms will be absorbed once they flow into grain boundaries. At the same time, it is also a reasonable assumption that the capacity of grain boundaries is big enough to absorb all the solute atoms since this simulation only focuses on the early stage of particle coarsening. The slopes at time step 8001 and time step 9001 in the concentration profile in Figure 3.3 (b) become obvious, which means that solute atoms start flowing into grain boundaries. As a result, matrix concentration near

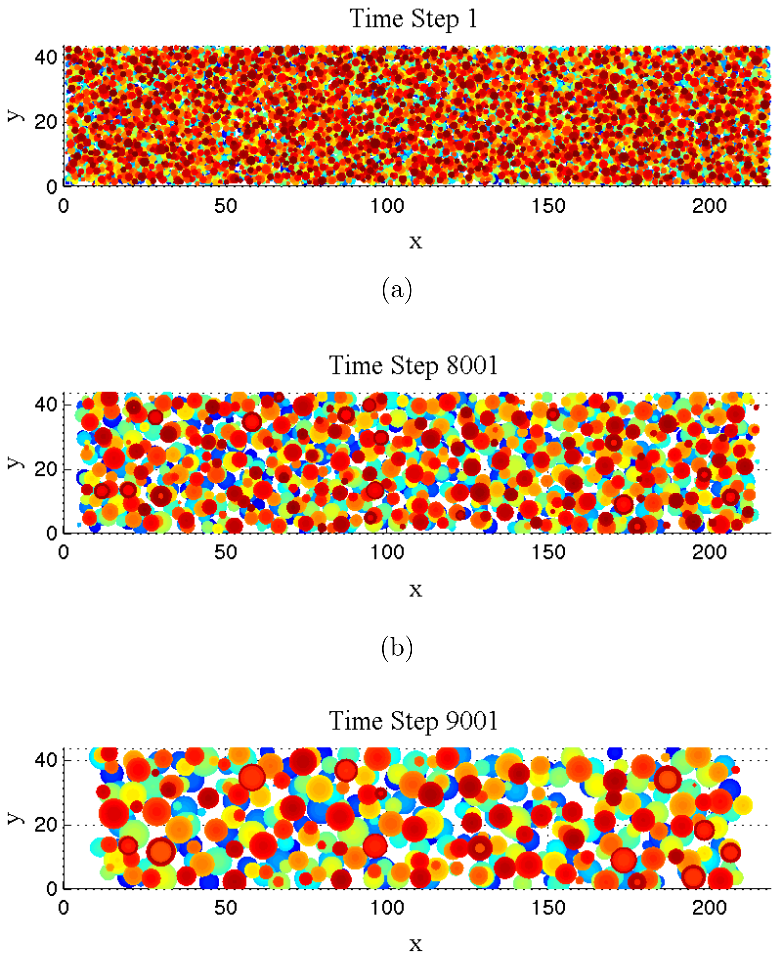

(a)

(b)

(c)

Figure 3.3: Horizontal view of particle coarsening near grain boundaries. 10,000 particles are initially distributed in the system without overlapping. Grain boundaries are perpendicular to x-axis, and located at $x = 0$ and $x = 218$. (a), (b), (c) illustrate the situations that are after time step 1, 8001 and 9001.

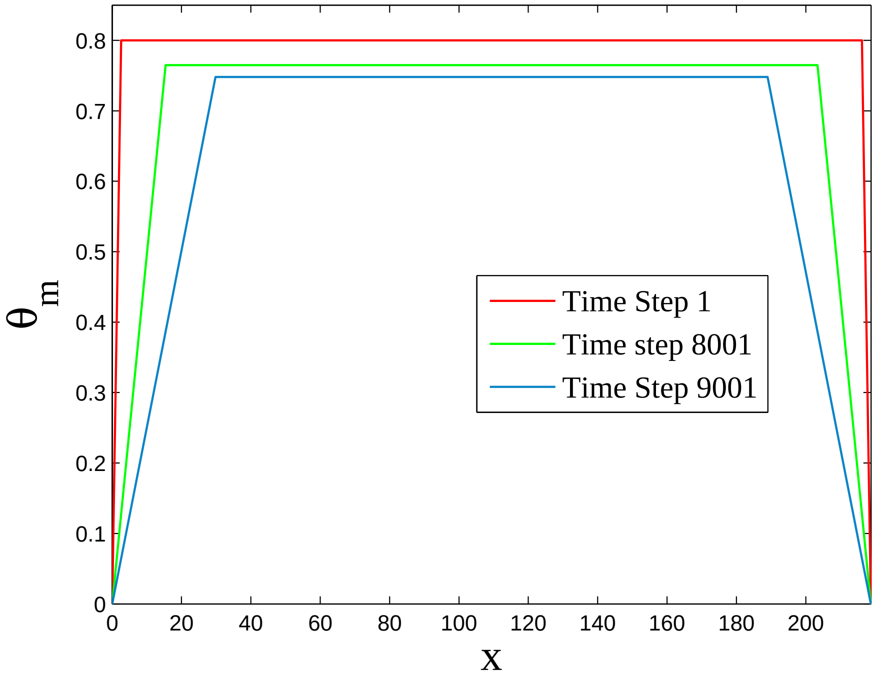

Figure 3.4: Concentration profile of 10,000-partice system at different time steps

grain boundaries decreases.

It should be noted that concentration in the matrix away from grain boundaries is position independent. This is why the horizontal line in the concentration profile of every image is straight. It is an ideal and reasonable assumption as well since the bulk matrix could be treated without the influence of grain boundaries due to being far away from grain boundaries. The concentration of bulk matrix is only time dependent. The concentration decreases gradually from time step 1 to time step 9001 since the average size of the particles increases. In other words the average curvature of the particles decreases which means the Gibbs-Thomson effect is less effective. Therefore, the equilibrium matrix concentration shifts to the less amount of solute atoms in the matrix.

3.2.2 Factors that influence the growth rate of particles near grain boundaries

Based on the mathematical model, four factors influence the growth rate of particles near grain boundaries: a) Volume fraction of second phase, b) diffusional interactions between particles, c) matrix diffusion and d) grain boundary diffusion.

The initialization of the system in the simulation reflects the influence of volume fraction of second phase, diffusional interactions between particles and matrix diffusion. To be more specific, they are three terms in Eq. 1.23, which are initial matrix concentration Θ_0, distance between two particles $\mid \vec{r_i} - \vec{r_j} \mid$ and matrix concentration $\Theta_m(\tau)$. All of these three factors have the same influence as discussed in Section 3.1.

The size of the domain which is under influence of grain boundary is time dependant. The progress rate of this domain, where flow of solute atoms toward grain boundary starts, $\frac{dx}{d\tau}$, is the key implementation of this mathematical model. It is given in Eq. 2.28, which mainly shows the influence of matrix diffusion and grain boundary diffusion on the growth rate of particles.

The calculation of $\frac{dx}{d\tau}$ is part of the calculation of matrix concentration $\Theta_m(\tau)$ during the simulation process. Notably, there are four terms in Eq. 2.28, where x is the x location of turning point in the concentration profile at the previous time step, $\frac{d\Theta_m}{d\tau}$ is the change of concentration of bulk matrix from previous time step to current time step , $\Theta_m(\tau)$ is concentration of bulk matrix of previous time step , and $\sum\limits_i \rho_i^2 \frac{d\rho_i}{d\tau}$ is total flux of solute atoms towards grain boundary of previous time step.

All of these four terms should be considered together since they represent the overall influence of grain boundaries. The grain boundary acts like a sink. As a result, all the solute atoms that flow toward grain boundaries will be absorbed directly. Based on solute atoms conservation, the number of solute atoms that flow to grain boundaries could be calculated. It is also the number of solute atoms that the system loses. At the same time, there is particle coarsening in the bulk matrix without the influence of grain boundaries. The method for calculation of $\Theta_m(\tau)$ at each time step is the same as the method explained in section 3.1. In this sense, we build a concentration profile for the whole system for each time step. If necessary, the concentration profile for a particular snapshot could be captured as well. Additionally, we could get particle size distribution and growth rate of each particle for this particular moment. From this point of view, the mathematical model for particle coarsening is effective and accurate.

3.2.3 Boardening rate of precipitation free zones

As what has been shown in Figure 3.3, PFZs form along grain boundaries during the process of particle coarsening. There are interactions between grain boundaries and solute atoms which influence solute atoms near grain boundaries more effectively compared with the ones inside the grain. As a result, solute atoms of particles near grain boundaries are absorbed by grain boundaries leading to the dissolution of particles near grain boundaries. As time goes by, a zone that is free of particles forms at the vicinity of grain boundaries. As shown in Figure 3.3, this zone becomes wider as time goes on.

Figure 3.5 shows the boardening rate of PFZs. It should be noted that the square of the scaled width of PFZs (W_p^2) with respect to scaled transformation time (τ) is illustrated in Figure 3.5. The solid line is the original line of 9,878 data points from

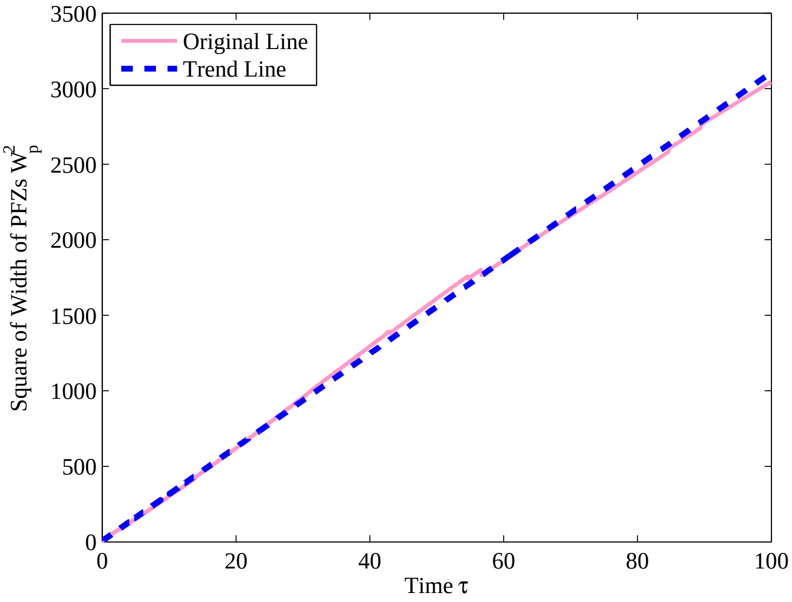

Figure 3.5: Boardening rate of PFZs

simulation results, while the dashed line is the fit line as shown in Eq. 3.1. The trend line fits very well, which means the square of width of PFZs has linear relationship with time. In other words, the width of PFZs is proportional to square root of time.

$$W_p^2 = 31.01\tau \tag{3.1}$$

The diffusion distance is proportional to square root of time as shown in Eq. 1.9. The striking similarities between these two relationships could help us explain the formation of PFZs. It reveals that the way in which solute atoms flow to grain boundaries follows diffusion theory. In other words, diffusion of solute atoms near grain boundaries causes the formation of PFZs.

The influence of volume fractions of second phase on PFZ broadening phenomenon is shown in Figure 3.6. In these simulations the volume fraction of the second phase

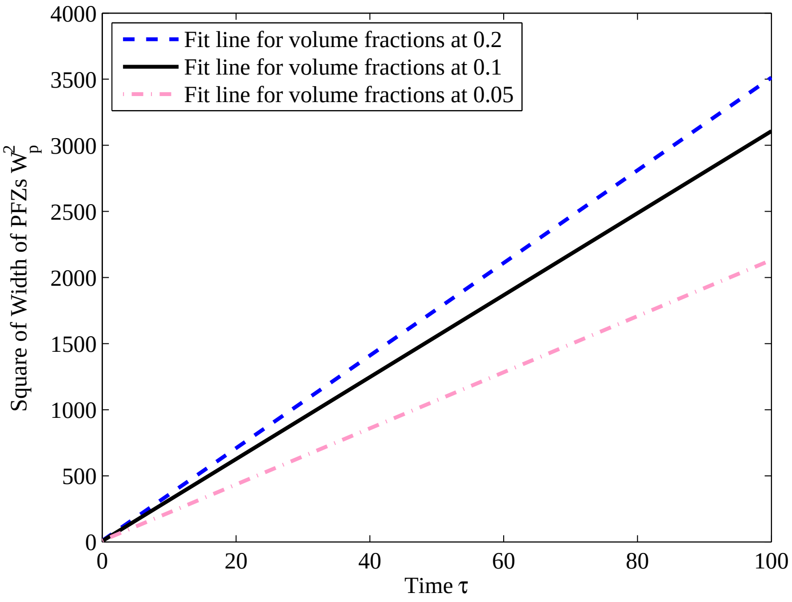

Figure 3.6: Boardening rate of PFZs for different volume fractions

are 0.05, 0.1 and 0.2 where results in the τ vs W_p^2 lines with the slope of 21.23, 31.01 and 35.03, respectively.

Therefore an obvious increase in the slopes is observed by increasing the volume fractions of second phase. This changing trend does make sense since concentration gradients of solute atoms are greater as the volume fractions of particles increase. It also can be another reason that this transformation is governed by diffusion phenomenon.

In addition, the mathematical model based on BEM shows the influence of volume factions of second phase, which fails to be shown in MFM [32, 33]. This is because MFM ignores solute atoms in the particles as well as the volume fractions of particles. As a consequence, even though MFM is effective in merging the bulk matrix, BEM is more accurate than MFM in simulating particle coarsening in alloys.

3.2.4 Particle size distribution near grain boundaries

Figure 3.7 shows the coarsening of 40,000 particles inside a grain between two paralleled grain boundaries from the horizontal view. For improving the simulation statistically, the length of the system is saved the same as the simulation box in Figure 3.3 while the cross section area is increased by a factor of 4. Therefore, the average number of particles in the unit of volume is the same. However, we can average the particle size over a larger number of particles. Figure 3.7 (a) shows the initial state of the whole system. Figure 3.7 (b) shows the late stage of particle coarsening process. We can see that particle size becomes larger whereas PFZs form along two paralleled grain boundaries.

Figure 3.8 is the statistical analysis of average particle size results from discretizing the domain into bin along x direction. In Figure 3.8 (a), we can see the homogenous particle size distribution at the initial stage of simulation. The average particle size in each bin at time step 5001 is a little larger than that at time step 1, which reflects that particles grow gradually. Later, for time step 20001, 22001, 24001 and 26001, the average particle size becomes much larger as time goes by. Notably, there are two small bulges near two paralleled grain boundaries of each time step, which represents the larger average particle size in these two zones compared with that in the middle of this grain.

Figure 3.8 (b) looks into the details of the area at top left in Figure 3.8 (a) which is highlighted by the rectangular. The peak of each time step is located along PFZs, which means particles near PFZs are larger than those inside the grain. Due to concentration gradient, particles near grain boundaries tend to dissolve leading to the formation of PFZs. As a result, most of solute atoms from particles diffuse

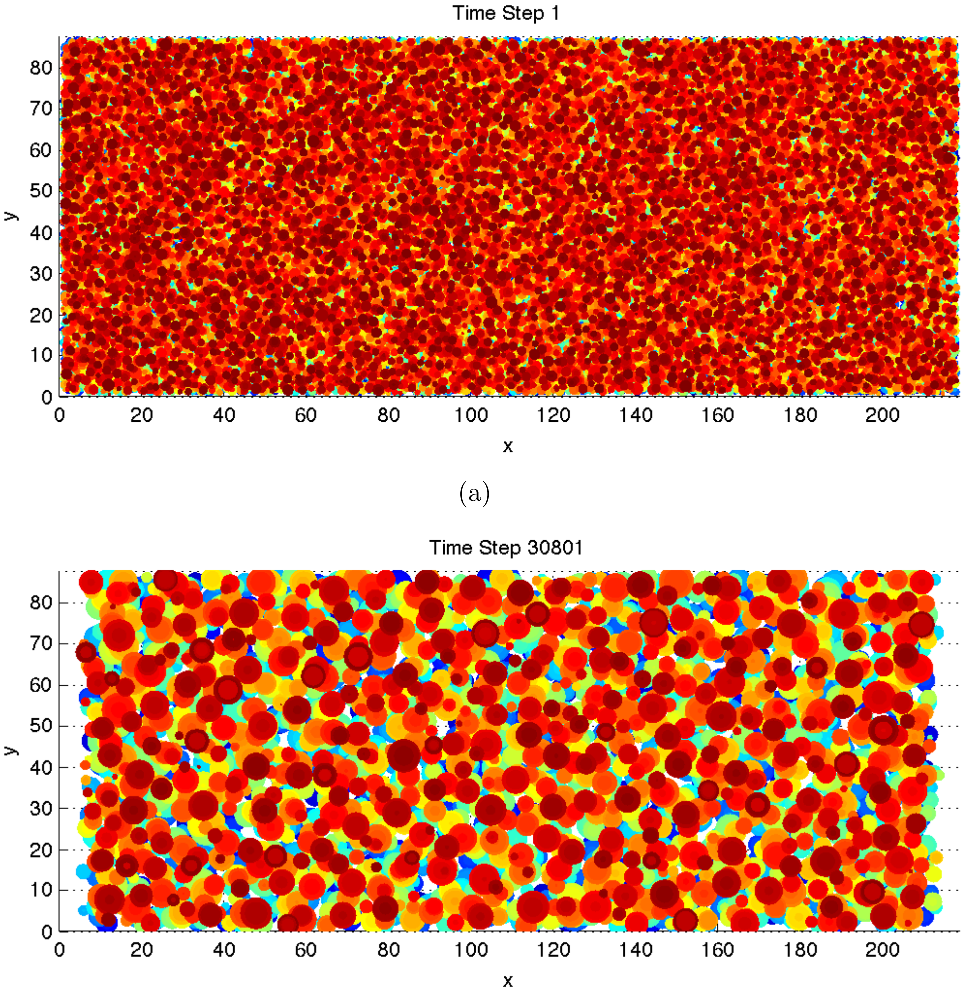

(a)

(b)

Figure 3.7: Horizontal view of particle coarsening between two paralleled grain boundaries inside a grain. 40,000 particles are initially distributed in the system without overlapping. Grain boundaries are perpendicular to x-axis, and located at $x = 0$ and $x = 218$. (a) and (b) illustrate the situations that are after time step 1 and 30801.

to grain boundaries, while a small percentage of solute atoms attach to particles at the edge of PFZs. This is because there is also a concentration gradient between these particles at the edge of PFZs and matrix in PFZs. Since particles along PFZs have more resources of solute atoms than those inside the grain far away from grain boundaries, the absolute value of growth rate of these particles is higher. In other words, it is faster for large particles to grow and small particles to dissolve along PFZs. And this is why the average particle size is larger along PFZs.

In addition, this feature has been observed in experimental examinations [53] as well. Thus, simulation results agree well with experimental results. Again, it proves that the mathematical model based on MFM, BEM, solute atoms conservation and diffusion theory has practical meaning in the field of particle coarsening.

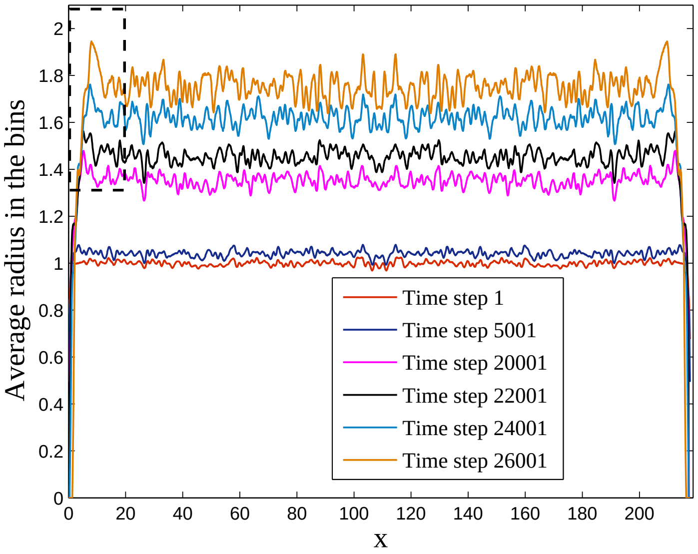

(a)

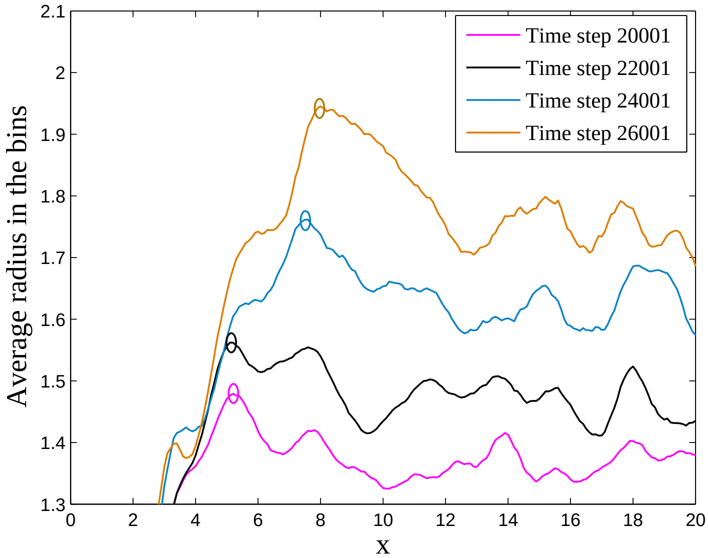

(b)

Figure 3.8: Average particle size during particle coarsening process. (a) shows the average particle size along x axis. (b) looks into the details of the area at top left in (a).

Chapter 4

Conclusions

In this dissertation, we simulated particle-coarsening process based on Mean Field Method and Boundary Element Method. At the same time, we demonstrated the capability and robustness of the mathematical model. Simulation results showed that Boundary Element Method is more reliable than Mean Field Method when applied in particle coarsening. Boundary Element Method is however limited to describing particle coarsening that is far away from grain boundaries.

Our primary work is that we successfully extended Boundary Element Method to particle coarsening near grain boundaries. Based on solute atoms conservation and diffusion theory, a major improvement was made to the previous mathematical model. And we demonstrated the capability and validity of the novel model using a binary alloy system. The simulation results are shown to quantitatively reproduce the essential features of particle coarsening as follows.

Firstly, precipitates free zones form near grain boundaries. We employed 10,000 and 40,000 particles at volume fraction 0.1 in two separate systems. And we employed 10,000 particles at volume fraction 0.05 and 0.2, respectively. Precipitates free zones form clearly near grain boundaries in all the systems. The model was shown to be well suited in describing particle coarsening near grain boundaries in alloys. Since we built the mathematical model according to diffusion theory, it proves the credibility of the theory, which is, the formation of precipitates free zones near grain boundaries is caused by diffusion of solute atoms.

Secondly, the width of precipitates free zones is proportional to square root of time. As we know, diffusion distance is proportional to square root of time. The striking similarities between these two relationships reveal the accuracy of our simulations.

Last but not the least, particles at the edge of precipitates free zones are larger than those inside the grain. This feature agrees well with experimental examinations. On the other hand, this feature could be explained by diffusion of solute atoms. Therefore, it also proves that the formation of precipitates free zones is caused by diffusion of solute atoms.

Chapter 5

Future work

Lots of work could be done in the future to improve the mathmatical model in order to make it universally applicable. The most beneficial work in the model that could be developed in the future is summarized as follows.

By recalling Figure 2.2, we can see that the focus of this dissertation is mainly on the calculation of $\frac{dx}{d\tau}$. In this way, a new concentration profile is built for each time step. It is worthwhile to point out here that it is an assumption that the capacity of grain boundaries to absorb solute atoms is unlimited. It is a reasonable assumption at the early stage of particle coarsening where we studied. However, the concentration of solute atoms cannot be always zero as more solute atoms are absorbed.

In this sense, a time dependent function of concentration at grain boundaries could be proposed. Thus, the whole concentration profile might be changed as well. A new concentration profile could be built for each time step. And at the same time, it is not only time dependent, but also depends on the area of grain boundaries, the type of grain boundaries, etc.

Bibliography

[1] TM Yue, HU Ha, and NJ Musson. Grain size effects on the mechanical properties of some squeeze cast light alloys. *Journal of materials science*, 30(9):2277–2283, 1995.

[2] K Kubota, M Mabuchi, and K Higashi. Review processing and mechanical properties of fine-grained magnesium alloys. *Journal of Materials Science*, 34(10):2255–2262, 1999.

[3] Arne K Dahle, Young C Lee, Mark D Nave, Paul L Schaffer, and David H StJohn. Development of the as-cast microstructure in magnesium–aluminium alloys. *Journal of light metals*, 1(1):61–72, 2001.

[4] YC Lee, AK Dahle, and DH StJohn. Grain refinement of magnesium. *Magnesium Technology*, 2000:211–218, 2000.

[5] EA Starke Jr and JT Staley. Application of modern aluminum alloys to aircraft. *Progress in Aerospace Sciences*, 32(2):131–172, 1996.

[6] HJ McQueen and OC Celliers. Application of hot workability studies to extrusion processing. part iii: physical and mechanical metallurgy of al–mg–si and al–zn–mg alloys. *Canadian metallurgical quarterly*, 36(2):73–86, 1997.

[7] EJ Lavernia, JD Ayers, and TS Srivatsan. Rapid solidification processing with specific application to aluminium alloys. *International materials reviews*, 37(1):1–44, 1992.

[8] Merton C Flemings. Solidification processing. *Metallurgical Transactions*, 5(10):2121–2134, 1974.

[9] PS Mohanty and JE Gruzleski. Mechanism of grain refinement in aluminium. *Acta Metallurgica et Materialia*, 43(5):2001–2012, 1995.

[10] Zenji Horita, Takayoshi Fujinami, Minoru Nemoto, and Terence G Langdon. Equal-channel angular pressing of commercial aluminum alloys: grain refinement, thermal stability and tensile properties. *Metallurgical and Materials Transactions A*, 31(3):691–701, 2000.

[11] T Khan and P Caron. Effect of heat treatments on the creep behaviour of a ni-base single crystal superalloy. *ONERA, TP*, (1983):7, 1983.

[12] MV Nathal and LJ Ebert. The influence of cobalt, tantalum, and tungsten on the elevated temperature mechanical properties of single crystal nickel-base superalloys. *Metallurgical Transactions A*, 16(10):1863–1870, 1985.

[13] DD Pearson and FD Lemkey. United technologies research center, e. *Hartford, CT, unpublished research*, 1983.

[14] AJ Ardell and RB Nicholson. On the modulated structure of aged ni-al alloys: with an appendix on the elastic interaction between inclusions by jd eshelby cavendish laboratory, university of cambridge, england. *Acta Metallurgica*, 14(10):1295–1309, 1966.

[15] H Gleiter and E Hornbogen. Precipitation hardening by coherent particles. *Materials Science and Engineering*, 2(6):285–302, 1968.

[16] Eckhard Nembach and Günter Neite. Precipitation hardening of superalloys by ordered γ-particles. *Progress in Materials Science*, 29(3):177–319, 1985.

[17] W Mangen and E Nembach. The effect of grain size on the yield strength of the $\gamma\prime$-hardened superalloy nimonic pe16. *Acta Metallurgica*, 37(5):1451–1463, 1989.

[18] CKL Davies, P Nash, and RN Stevens. Precipitation in ni-co-al alloys. *Journal of Materials Science*, 15(6):1521–1532, 1980.

[19] CS Jayanth and Philip Nash. Factors affecting particle-coarsening kinetics and size distribution. *Journal of materials science*, 24(9):3041–3052, 1989.

[20] JA Marqusee and John Ross. Theory of ostwald ripening: Competitive growth and its dependence on volume fraction. *The Journal of chemical physics*, 80(1):536–543, 1984.

[21] Kenneth D Gibson and Harold A Scheraga. Exact calculation of the volume and surface area of fused hard-sphere molecules with unequal atomic radii. *Molecular Physics*, 62(5):1247–1265, 1987.

[22] M Fährmann, P Fratzl, O Paris, E Fährmann, and William C Johnson. Influence of coherency stress on microstructural evolution in model ni-al-mo alloys. *Acta metallurgica et materialia*, 43(3):1007–1022, 1995.

[23] WJ Kim, JK Kim, TY Park, SI Hong, DI Kim, YS Kim, and JD Lee. Enhancement of strength and superplasticity in a 6061 al alloy processed by

equal-channel-angular-pressing. *Metallurgical and materials transactions A*, 33(10):3155–3164, 2002.

[24] TH Sanders Jr and El A Starke Jr. The effect of slip distribution on the monotonic and cyclic ductility of al li binary alloys. *Acta Metallurgica*, 30(5):927–939, 1982.

[25] David A Porter and Kenneth E Easterling. *Phase Transformations in Metals and Alloys, (Revised Reprint).* CRC press, 1992.

[26] Michel Perez. Gibbs–thomson effects in phase transformations. *Scripta materialia*, 52(8):709–712, 2005.

[27] Jeffrey J Hoyt. *Phase transformations.* McMaster University Bookstore, 2011.

[28] William D Callister and David G Rethwisch. *Materials science and engineering: an introduction*, volume 7. Wiley New York, 2007.

[29] WZ Ostwald. Blocking of ostwald ripening allowing long-term stabilization. *Z. Phys. Chem.*, 37:385, 1901.

[30] Peter W Voorhees. The theory of ostwald ripening. *Journal of Statistical Physics*, 38(1-2):231–252, 1985.

[31] GW Greenwood. The growth of dispersed precipitates in solutions. *Acta Metallurgica*, 4(3):243–248, 1956.

[32] Ilya Mikhailovich Lifshitz and Vitaly V Slyozov. The kinetics of precipitation from supersaturated solid solutions. *Journal of Physics and Chemistry of Solids*, 19(1):35–50, 1961.

[33] Carl Wagner. Theorie der alterung von niederschlägen durch umlösen (ostwald-reifung). *Zeitschrift für Elektrochemie, Berichte der Bunsengesellschaft für physikalische Chemie*, 65(7-8):581–591, 1961.

[34] LP Pitaevskii and EM Lifshitz. *Physical kinetics*, volume 10. Butterworth-Heinemann, 1981.

[35] AJ Ardell. The effect of volume fraction on particle coarsening: theoretical considerations. *Acta metallurgica*, 20(1):61–71, 1972.

[36] K Tsumuraya and Y Miyata. Coarsening models incorporating both diffusion geometry and volume fraction of particles. *Acta Metallurgica*, 31(3):437–452, 1983.

[37] R Asimow. Clustering kinetics in binary alloys. *Acta Metallurgica*, 11(1):72–73, 1963.

[38] AD Brailsford and P Wynblatt. The dependence of ostwald ripening kinetics on particle volume fraction. *Acta Metallurgica*, 27(3):489–497, 1979.

[39] PW t Voorhees and ME Glicksman. Solution to the multi-particle diffusion problem with applications to ostwald ripeningi. theory. *Acta metallurgica*, 32(11):2001–2011, 1984.

[40] PETER W Voorhees and ME Glicksman. Solution to the multi-particle diffusion problem with applications to ostwald ripeningii. computer simulations. *Acta Metallurgica*, 32(11):2013–2030, 1984.

[41] Michio Tokuyama, Kyozi Kawasaki, and Yoshihisa Enomoto. Kinetic equations for ostwald ripening. *Physica A: Statistical Mechanics and its Applications*, 134(2):323–338, 1986.

[42] Gurpreet Grewal and Sreeramamurtha Ikem. Particle coarsening behavior of α-β titanium alloys. *Metallurgical Transactions A*, 21(6):1645–1654, 1990.

[43] H Gleiter and E Hornbogen. The formation of coherent ordered precipitates in a ni-cr-al-alloy(coherent ordered precipitates formation in ni- cr-al alloy, discussing spacing, shape and size of gamma prime particles as function of time). *ZEITSCHRIFT FUER METALLKUNDE*, 58:157–163, 1967.

[44] TB Gibbons and BE Hopkins. The influence of grain size and certain precipitate parameters on the creep properties of ni-cr-base alloys(grain size and precipitate parameters effect on creep properties of ni-cr alloys). *Metal Science Journal*, 5:233–240, 1971.

[45] AJ Ardell. An application of the theory of particle coarsening: The γ'precipitate in ni al alloys. *Acta Metallurgica*, 16(4):511–516, 1968.

[46] DJ Chellman and AJ Ardell. The coarsening of γ'precipitates at large volume fractions. *Acta Metallurgica*, 22(5):577–588, 1974.

[47] V Biss and DL Sponseller. The effect of molybdenum on γ coarsening and on elevated-temperature hardness in some experimental nickel-base superalloys. *Metallurgical Transactions*, 4(8):1953–1960, 1973.

[48] RA MacKay and MV Nathal. γ coarsening in high volume fraction nickel-base alloys. *Acta Metallurgica et Materialia*, 38(6):993–1005, 1990.

[49] TH Courtney. Microstructural evolution during liquid phase sintering: Part i. development of microstructure. *Metallurgical Transactions A*, 8(5):679–684, 1977.

[50] TH Courtney. Microstructural evolution during liquid phase sintering: Part ii. microstructural coarsening. *Metallurgical Transactions A*, 8(5):685–689, 1977.

[51] WC Johnson, TA Abinandanan, and PW Voorhees. The coarsening kinetics of two misfitting particles in an anisotropic crystal. *Acta Metallurgica et Materialia*, 38(7):1349–1367, 1990.

[52] CS Jayanth and Philip Nash. Factors affecting particle-coarsening kinetics and size distribution. *Journal of materials science*, 24(9):3041–3052, 1989.

[53] M Raghavan. Microanalysis of precipitate free zones (pfz) in al-zn-mg and cu-ni-nb alloys. *Metallurgical Transactions A*, 11(6):993–999, 1980.

[54] M Abe, K Asano, and A Fujiwara. Influence of the precipitate-free zone width on the tensile properties of an al-6 wt pct zn-1.2 wt pct mg alloy. *Metallurgical Transactions*, 4(6):1499–1505, 1973.

[55] Tomo Ogura, Shoichi Hirosawa, and Tatsuo Sato. Quantitative characterization of precipitate free zones in al–zn–mg (–ag) alloys by microchemical analysis and nanoindentation measurement. *Science and Technology of Advanced Materials*, 5(4):491–496, 2004.

[56] MJ Starink, P Wang, I Sinclair, and PJ Gregson. Microstrucure and strengthening of al–li–cu–mg alloys and mmcs: I. analysis and modelling of microstructural changes. *Acta materialia*, 47(14):3841–3853, 1999.

[57] WA Cassada, GJ Shiflet, and EA Starke. Grain boundary precipitates with five-fold diffraction symmetry in an al li cu alloy. *Scripta metallurgica*, 20(5):751–756, 1986.

[58] P Doig and JW Edington. Influence of precipitate free zones on the stress corrosion susceptibility of a ternary al-5.9 wt% zn-3.2 wt% mg alloy. *Corrosion*, 31(10):347–352, 1975.

[59] DE ward and GM Lorimer. In *Proc. of 3rd International Conf. on Strength of Metals and Alloys*, volume 1, page 488. Institute of Metals, 1973.

[60] KV Jata, KK Sankaran, and JJ Ruschau. Friction-stir welding effects on microstructure and fatigue of aluminum alloy 7050-t7451. *Metallurgical and Materials Transactions A*, 31(9):2181–2192, 2000.

[61] Thorsten Krol, Dietmar Baither, and Eckhard Nembach. The formation of precipitate free zones along grain boundaries in a superalloy and the ensuing effects on its plastic deformation. *Acta materialia*, 52(7):2095–2108, 2004.

[62] SC Jha, TH Sanders, and MA Dayananda. Grain boundary precipitate free zones in al-li alloys. *Acta Metallurgica*, 35(2):473–482, 1987.

[63] DP Yao, YZ Zhang, ZQ Hu, YY Li, and CX Shi. The formation and growth of pfz at grain boundary in al-11.9 at.-% li alloy. *Scripta metallurgica*, 23(4):537–541, 1989.

[64] TK Vaidyanathan and K Mukherjee. Continuous precipitation in cu-rich cu-ti binary and cu-ti-al ternary alloys. *Journal of Materials Science*, 10(10):1697–1710, 1975.

[65] Hiroyuki Toda, Toshiro Kobayashi, and Mitsuo Niinomi. Effects of aging treatments on fracture characteristics of 6061 aluminum-alloy reinforced with sic whisker. *JOURNAL OF THE JAPAN INSTITUTE OF METALS*, 58(4):468–475, 1994.

[66] Nils Ryum. The influence of a precipitate-free zone on the mechanical properties of an al-mg-zn alloy. *Acta Metallurgica*, 16(3):327–332, 1968.

[67] PN Adler, R Delasi, and Gary Geschwind. Influence of microstructure on the mechanical. *Metallurgical Transactions*, 3(12):3191–3200, 1972.

[68] SP Ringer, K Hono, and T Sakurai. The effect of trace additions of sn on precipitation in al-cu alloys: an atom probe field ion microscopy study. *Metallurgical and Materials Transactions A*, 26(9):2207–2217, 1995.

[69] Tomo Ogura, Shoichi Hirosawa, Alfred Cerezo, and Tatsuo Sato. Atom probe tomography of nanoscale microstructures within precipitate free zones in al–zn–mg (–ag) alloys. *Acta Materialia*, 58(17):5714–5723, 2010.

[70] JK Park and AJ Ardell. Microchemical analysis of precipitate free zones in 7075-a1 in the t6, t7 and rra tempers. *Acta metallurgica et materialia*, 39(4):591–598, 1991.

[71] Sunil Chandra Jha. Precipitation processes in al-li and al-li-mg alloys. 1987.

[72] H Okuda and S Ochiai. A monte carlo simulation on pfz formation in a model binary alloy. In *Materials Forum*, volume 28, pages 152–157, 2004.

[73] Hiroshi Okuda and Shojiro Ochiai. A monte carlo simulation on the pfz microstructures in al-based alloys during multistep annealing. In *Materials Science Forum*, volume 475, pages 937–940. Trans Tech Publ, 2005.

[74] Ola Jensrud and Nils Ryum. The development of microstructures in al li alloys. *Materials Science and Engineering*, 64(2):229–236, 1984.

[75] B Cai, BL Adams, and TW Nelson. Relation between precipitate-free zone width and grain boundary type in 7075-t7 al alloy. *Acta materialia*, 55(5):1543–1553, 2007.

[76] AF Giamei and DL Anton. Rhenium additions to a ni-base superalloy: effects on microstructure. *Metallurgical transactions A*, 16(11):1997–2005, 1985.

[77] Nicholas Metropolis and Stanislaw Ulam. The monte carlo method. *Journal of the American statistical association*, 44(247):335–341, 1949.

[78] Pierre Weiss. L'hypothèse du champ moléculaire et la propriété ferromagnétique. *J. Phys. Theor. Appl.*, 6(1):661–690, 1907.

[79] Jun S Liu and Rong Chen. Sequential monte carlo methods for dynamic systems. *Journal of the American statistical association*, 93(443):1032–1044, 1998.

[80] SY Chang, VR Pandharipande, J Carlson, and KE Schmidt. Quantum monte carlo studies of superfluid fermi gases. *Physical Review A*, 70(4):043602, 2004.

[81] Daan Frenkel and Anthony JC Ladd. New monte carlo method to compute the free energy of arbitrary solids. application to the fcc and hcp phases of hard spheres. *The Journal of chemical physics*, 81(7):3188–3193, 1984.

[82] Manfred Opper and David Saad. *Advanced mean field methods: Theory and practice*. MIT press, 2001.

[83] G Bouzerar, J Kudrnovskỳ, Lars Bergqvist, and Patrick Bruno. Ferromagnetism in diluted magnetic semiconductors: A comparison between ab initio mean-field, rpa, and monte carlo treatments. *Physical Review B*, 68(8):081203, 2003.

[84] John Hertz. *Introduction to the theory of neural computation*, volume 1. Basic Books, 1991.

[85] Hidetoshi Nishimori. *Statistical physics of spin glasses and information processing*, volume 187. Oxford University Press Oxford, 2001.

[86] Michael I Jordan, Zoubin Ghahramani, Tommi S Jaakkola, and Lawrence K Saul. An introduction to variational methods for graphical models. *Machine learning*, 37(2):183–233, 1999.

[87] Nicolas Vandewalle and Marcel Ausloos. Self-organized criticality in phylogenetic-like tree growths. *Journal de Physique I*, 5(8):1011–1025, 1995.

[88] DH Lenschow, J Co Wyngaard, and Wo To Pennell. Mean-field and second-moment budgets in a baroclinic, convective boundary layer. *Journal of the Atmospheric Sciences*, 37(6):1313–1326, 1980.

[89] Trond Grenager, Dan Klein, and Christopher D Manning. Unsupervised learning of field segmentation models for information extraction. In *Proceedings of the 43rd annual meeting on association for computational linguistics*, pages 371–378. Association for Computational Linguistics, 2005.

[90] James A Davis and Jonathan Jedwab. Peak-to-mean power control in ofdm, golay complementary sequences, and reed-muller codes. *Information Theory, IEEE Transactions on*, 45(7):2397–2417, 1999.

[91] David Ruelle. *Statistical mechanics*, volume 3. Benjamin New York, 1969.

[92] JJ Hoyt. A mean field description of the kinetics of precipitate free zone formation. *Scripta materialia*, 37(12):2033–2039, 1997.

[93] Ruben Scardovelli and Stéphane Zaleski. Direct numerical simulation of free-surface and interfacial flow. *Annual Review of Fluid Mechanics*, 31(1):567–603, 1999.

[94] Yiannis Ventikos and George Tzabiras. A numerical method for the simulation of steady and unsteady cavitating flows. *Computers & Fluids*, 29(1):63–88, 2000.

[95] Qing-Hua Qin. *The Trefftz finite and boundary element method*. Computational Mechanics, 2000.

[96] R Criado, Leonard J Gray, V Mantič, and Federico París. Green's function evaluation for three-dimensional exponentially graded elasticity. *International journal for numerical methods in engineering*, 74(10):1560–1591, 2008.

[97] CA Brebbia, JCF Telles, and LC Wrobel. Potential problems. In *Boundary Element Techniques*, pages 47–108. Springer, 1984.

[98] James H Kane. Boundary element analysis in engineering continuum mechanics(book). *Englewood Cliffs, NJ: Prentice Hall, 1994.*, 1994.

[99] CA Brebbia and AJ Nowak. Solving heat transfer problems by the dual reciprocity bem. In *Boundary Element Methods in Heat Transfer*, pages 1–31. Springer, 1992.

[100] Weifeng Tang. *Transforming domain into boundary integrals in BEM: a generalized approach*, volume 35. Springer Berlin/Heidelberg, 1988.

[101] D Nardini and CA Brebbia. The solution of parabolic and hyperbolic problems using an alternative boundary element formulation. *Boundary elements VII*, pages 3–87, 1985.

[102] D Nardini and CA Brebbia. Boundary integral formulation of mass matrices for dynamic analysis. In *Time-dependent and Vibration Problems*, pages 191–208. Springer, 1985.

[103] D Nardini and CA Brebbia. The solution of parabolic and hyperbolic problems using an alternative boundary element formulation. *Boundary elements VII*, pages 3–87, 1985.

[104] LC Wrobel, CA Brebbia, and D Nardini. Analysis of transient thermal problems in the beasy system. *BETECH*, 86:269–280, 1986.

[105] CA Brebbia and LA Wrobel. The solution of parabolic problems using the dual reciprocity boundary element. In *Advanced boundary element methods*, pages 55–71. Springer, 1988.

[106] Phillip M Morse and Herman Feshbach. Methods of theoretical physics, international series in pure and applied physics. *New York: McGraw-Hill*, 1(1953):29, 1953.

[107] HS Carslaw and JC Jaeger. Conduction of heat in solids, 2nd edn clarendon press, 1959.

[108] YP Chang, CS Kang, and David J Chen. The use of fundamental green's functions for the solution of problems of heat conduction in anisotropic media. *International Journal of Heat and Mass Transfer*, 16(10):1905–1918, 1973.

[109] Richard Paul Shaw. An integral equation approach to diffusion. *International Journal of Heat and Mass Transfer*, 17(6):693–699, 1974.

[110] LC Wrobel and CA Brebbia. The boundary element method for steady-state and transient heat conduction. *Numerical Methods in Thermal Problems*, 1, 1979.

[111] Norio Akaiwa and PW Voorhees. Late-stage phase separation: dynamics, spatial correlations, and structure functions. *Physical Review E*, 49(5):3860, 1994.

[112] B Noble and GE Thompson. Precipitation characteristics of aluminium-lithium alloys. *Metal Science*, 5(1):114–120, 1971.

[113] HM Tawancy. Precipitation characteristics of μ-phase in wrought nickel-base alloys and its effect on their properties. *Journal of materials science*, 31(15):3929–3936, 1996.

[114] GE Thompson and B Noble. Precipitation characteristics of aluminum-lithium alloys containing magnesium. *J. Inst. Met.*, 101(4):111–115, 1973.

[115] Stanisław Dymek and Marek Dollar. Tem investigation of age-hardenable al 2519 alloy subjected to stress corrosion cracking tests. *Materials Chemistry and Physics*, 81(2):286–288, 2003.